EVALUATION OF INDEPENDENT MESH MODELING FOR TEXTILE COMPOSITES

A Thesis

by

JEFFREY SCOTT MCQUIEN

Submitted to the Office of Graduate and Professional Studies of
Texas A&M University
in partial fulfillment of the requirements for the degree of

MASTER OF SCIENCE

Chair of Committee,	John D. Whitcomb
Committee Members,	Mohammad Naraghi
	Terry Creasy
Head of Department,	Rodney Bowersox

May 2017

Major Subject: Aerospace Engineering

ABSTRACT

The Independent Mesh Method (IMM) was used to analyze stress distributions within a unit cell model for a symmetrically stacked plain weave textile composite. Results from these analyses were compared to those of conventional finite element analyses, which are well established. Preliminary comparisons showed extreme disagreement between the two methodologies. Further investigation into the source of these differences led to significant corrections to the IMM implementation. After these updates, much better agreement between the two methodologies was observed; however, noticeable differences were still present. The remaining differences were characterized using a simple two-inclusion model upon which the impacts of the penalty displacement method, which the IMM relies upon heavily, were more apparent. It was shown that the implementation of the penalty displacement method for maintaining approximate displacement continuity between two surfaces induces significant error in stress distributions close to the interface. While these effects are less noticeable in the plain weave model, they are still present and diminish the fidelity of stress information in important tow-matrix interface regions, prohibiting the reliable prediction of damage initiation and growth.

DEDICATION

This thesis is dedicated to my father, without whom, it would have never been.

ACKNOWLEDGEMENTS

I sincerely appreciate the guidance of my adviser Dr. John Whitcomb. It has been a pleasure working under his leadership. I have ultimate respect for his capabilities as a researcher and teacher, as well as for his unwavering standards. The opportunity to work as his teaching assistant was a very enriching experience. In addition, I would like to thank the members of my committee, Dr. Mohammad Naraghi and Dr. Terry Creasy, for affording their time to see me through this education. I would also like to thank Dr. Darren Hartl for supporting me through, and helping provide the great experience of working on the morphing radiator research.

I greatly appreciate the help of the VTMS team at AFRL, Dr. David Mollenhauer, Dr. Endel Iarve, Eric Zhou, and Dr. Lauren Ferguson. I am thankful to have had the opportunity to work closely with them over the summer, where the close proximity allowed us to make significant progress.

My senior colleagues and fellow students Keith Ballard and Christopher Bertagne did more than their fair share of answering my questions, and I give my thanks to each. Keith has happily afforded himself as a resource, and I always know that if my question ends up reaching him, it will get answered.

Lastly, I would like to thank my mother for her everlasting support.

CONTRIBUTORS AND FUNDING SOURCES

This work was supported by a thesis committee consisting of Professors John Whitcomb (advisor and chair of committee) and Mohammad Naraghi of the Department of Aerospace Engineering, and Professor Terry Creasy of the Department of Materials Science and Engineering.

All work conducted for this thesis was completed by the student under the oversight of the thesis committee and Dr. David Mollenhauer, Dr. Endel Iarve, and Eric Zhou of the Air Force Research Laboratory.

TABLE OF CONTENTS

Page

LIST OF FIGURES

FIGURE Page

LIST OF TABLES

TABLE Page

1. INTRODUCTION

Composite materials require additional analysis efforts than more conventional engineering materials due to their inherently heterogeneous microstructures. Multiscale analysis methodologies have developed within the field of composites as one approach to address this requirement. Since a composite material is defined by the combination of one or more constituent materials, the resulting material usually has at least two material scales. The smallest scale is defined by the length scale of the smallest constituent, at which the material is heterogeneous, and the largest scale is defined by the length scale at which the composite appears homogeneous. Multiscale analysis is an approach in which results from analyses done at one scale are used to model the behavior of the material at another scale. The end goal of the effort is to understand the behavior of the composite enough such that it may be modeled without representation of its constituents. It would not be practical to discretely model every single reinforcement in a large concrete beam, or every carbon fiber in an aircraft skin. At each particular scale there may be several analysis methods available to choose from. These methods may be experimental, analytic, or numerical. Of course experimental methods, while the most realistic, are costly and require the most time. Analytic methods can be very accurate but are difficult to apply to complex structures. Numerical methods are the least expensive, and the least time consuming given modern developments in computer technology. However, numerical analyses are highly sensitive to the implementation of theory and to the parameters involved in describing material behavior. Because of this, numerical methods are developed and validated using experimental and analytic results. A validated numerical analysis framework can be used to analyze a much higher volume of problems

than its counterparts. The finite element method is a powerful numerical analysis framework capable of modeling at all material scales, and is the centerpiece of this work.

Fiber reinforced composites are a popular engineering material on which multiscale analysis is often performed. Whether or not the fiber reinforced composite is part of the unidirectional or textile class, the material scales can be defined by the hierarchical breakdown of the composite material. Unidirectional composite laminae, or mats, are made from the combination of fibers, that are all oriented in the same direction, and resin. In classical composite nomenclature, the resin is referred to as the matrix, and the fibers are referred to as the inclusions. These laminae are then stacked into the resulting composite laminate. In order to understand the properties of the laminate, the properties of the individual laminae must first be understood; this establishes the basis for multiscale analysis. On the other hand, textile, or woven fabric, composites require an additional level of analysis. Figure 1.1 depicts the hierarchical breakdown, or scales used in a multiscale approach, of a textile composite component. A textile composite weaving tows, which are a combination of fibers and resin, into a fabric mat. The resulting fabric mat can then be stacked in a manner similar to the laminae of a unidirectional laminate. In this case the lowest level of analysis is performed on the tow. Since the tow is a combination of unidirectional fibers and resin, this analysis scale, Figure 1.1a, is identical to the microscale analysis of the unidirectional fiber reinforced composites. The next scale, Figure 1.1b, is defined by the length scale of the textile weave and is known as the mesoscale. The mesoscale captures the effect of the weave morphology and contains woven tows, whose properties are determined by the microscale analysis, and pockets of pure resin. Mesoscale models are usually realized as unit cells, which capture all of the geometry necessary to describe the fabric. Lastly the macroscale, Figure 1.1c,

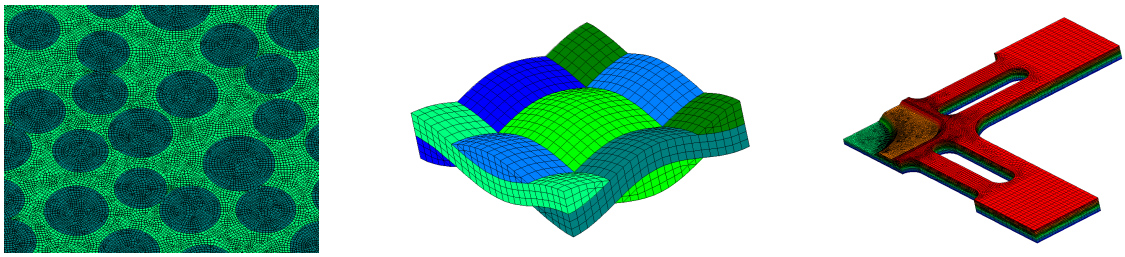

(a) Microscale (b) Mesoscale (c) Macroscale

Figure 1.1: Multi-scale analysis of textile composites

is the scale at which the composite material is homogenized and is used to model engineering parts. The present work is concerned with the geometric representation of the textile at the mesoscale, and its analysis using the finite element method.

Mesoscale modeling is particularly challenging due to the complex geometries inherent in woven fabrics. In order to perform finite element analysis on a model at this scale, the geometry must first be simulated and then discretized into a suitable finite element mesh. Figure 1.2 shows an in-plane view of a triaxial braided composite. Variability can be easily identified as tow widths change from tow-to-tow, as well as along the length of an individual tow. Furthermore, each tow has unique surface features which appear most frequently near the tow intersections. These characteristics make it extremely difficult to realistically simulate textile geometry. Consequentially, as geometry is more realistically simulated, its incorporation into a finite element model becomes more difficult, particularly the formulation of the finite element mesh.

Conventionally, the difficulty in accurately simulating mesoscale geometry is diminished by idealizing the tow architecture and weave pattern. This removes the randomness present in the textile as discussed previously. By idealizing the tow architecture it is possible to design a finite element mesh that fits each tow at every

Figure 1.2: In plane photograph of a triaxial braided fabric, reprinted from [1]

location. By idealizing the weave pattern it is possible to obtain mesh compatibility in a consistent manner throughout the finite element mesh. Idealizations of these characteristics usually result in tow cross sections approximated as biconvex, or elliptical, shapes, and sinusoidal tow paths. An early work based on this geometric approach is outlined in [2]. The geometric representation, and its impacts, of the analysis therein are thoroughly discussed in [3]. It is shown that the idealized geometry can be completely characterized by the chosen tow path as well as the cross sectional shape. All other model parameters are either directly or indirectly determined by these two characteristics. Much of the work in analysis of textile composites follows similarly. Obviously the idealization of textile geometric architecture may have some impact on the results predicted by the analysis. A detailed investigation into the effect of including geometric randomness inherent in textile composites has yet to be carried out. However, it has been shown in microscale analysis of fiber composites that the consideration of geometric randomness has a significant impact on results [4]. Mesoscale analyses lack a similar comparison due to the extreme difficulty associated with first simulating a realistic geometry, and then performing finite element analysis on it.

Recently a method was developed by Zhou et al. [5], which aims to simulate the

geometry of a textile composite at the mesoscale using a physics modeling technique based on the multi chain digital element technique [6]. The resulting textile architecture contains many features that are often observed in textiles, such as inconsistencies in weave pattern, varying tow thicknesses across the width, and varying tow cross sections along the tow path. The Virtual Textile Morphology Suite (VTMS), a textile analysis tool developed at the Air Force Research Laboratory (AFRL), is built around an implementation of this digital element technique. As stated previously, the difficulty in establishing a finite element mesh increases as the accuracy of geometric simulation increases. VTMS is paired to AFRL's B-Spline Analysis Method (BSAM) finite element code, which makes use of a combination of unconventional finite element techniques, referred to as the Independent Mesh Method (IMM), to address this issue [7][1]. First, each geometric *entity* is meshed independently and compatibility between adjacent surfaces is imposed through a penalty displacement method. A geometric entity is defined as a standalone body that is meshed independently from all other entities. This is analogous to a part within an assembly in many computer based design tools. In the context of textiles, each tow is an entity, as well as the body of pure resin. Second, the mesh representing the body of pure resin is generated using a technique similar to the extended finite element method (XFEM). In the IMM approach, the resin is first represented as a background rectangular structured grid mesh, with dimensions that encompass the volume of the tows. The elements of the resin are then restructured based on the regions occupied by tows. The shape functions of resin elements that are completely within the tows are disregarded, and those belonging to elements that are intersected by the boundary assume an adapted integration scheme. The portion of the element falling outside the

[1]The cited papers describe the original version of the IMM which makes use of a marching-cube integration mesh rather than tetrahedral

region occupied by the tow is supplemented with a set of integration points placed by the insertion of tetrahedral integration elements. The IMM is more general than its application to textiles, and as such may be described as choosing a set of geometric entities which act as *master* surfaces, from which the other (background) entities will be restructured as needed. In the case of the application to textiles, the tows are defined as the master surfaces.

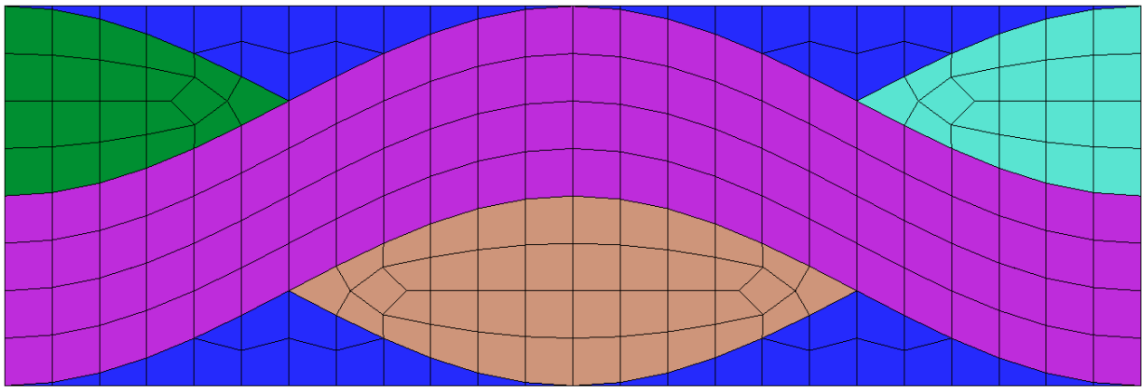

(a) Conventional plain weave unit cell using idealized geometry

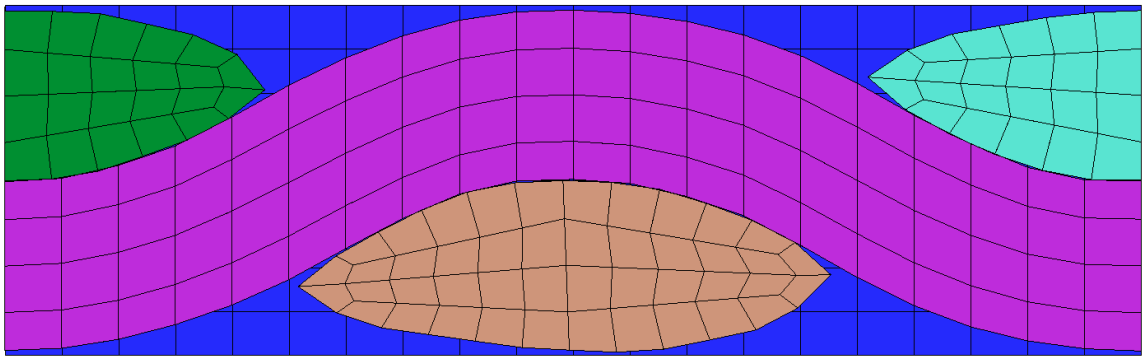

(b) IMM plain weave unit cell mesh of VTMS simulated geometry

Figure 1.3: Comparison of conventional and VTMS-IMM plain weave unit cell finite element models

A comparison of side views of conventional and VTMS-IMM finite element models

is shown in Figure 1.3. Figure 1.3a shows a conventional finite element model using idealized tow architectures. Each tow cross section is identical, and is constant along the undulation of the tow. The specific geometry shown is produced using a sweeping method rather than extruded, and has a relatively unrealistic waviness ratio [3]. There is perfect tow-to-tow and tow-to-resin mesh compatibility, as the entire domain is discretized into a single finite element mesh. Figure 1.3b shows a comparable IMM finite element model using tow architecture simulated by VTMS. Each tow cross section is unique, and is not constant along the tow path. There is no tow-to-tow or tow-to-resin nodal compatibility as each entity is meshed independently, and the resin mesh is approximated using the IMM described above.

These additional finite element methods, while may be essential to analyzing the realistic geometry produced by VTMS, may themselves introduce significant errors on material behavior predictions. The objective of this work is to understand what those impacts are, if any, and establish a method for minimizing them. The systematic evaluation of these potential impacts will be carried out by implementing the IMM on a model upon which a conventional finite element analysis may also be used. The conventional analysis will serve as the benchmark. As discussed, there are several factors that make the IMM approach different from that of a conventional finite element approach. The IMM approach:

- Is able to consider complex geometries without burdening the meshing process.
- Uses an unconventional element formulation to model the volumes of pure resin within the unit cell.
- Uses a penalty method to impose displacement continuity between separate, independent mesh entities, which may or may not have compatible surface meshes.

Regarding the above list, each item requires the use of the items below it given the implementation of the IMM. Since the evaluation performed in this work requires the use of a conventional analysis as benchmark, the first item can not be considered. The production of a compatible mesh for the VTMS simulated geometry, suitable for use with conventional finite elements, may in fact be possible, but the meshing process would be cumbersome. In addition, the IMM would not be necessary given a compatible mesh. As such, the current evaluation will focus on the implications of the IMM characteristics outlined in the second and third bullets. It is possible to invoke each of these IMM characteristics upon a textile model that is otherwise suitable for use with conventional finite element methods. The evaluations herein make use of identical geometries between conventional and IMM models. The meshes for master entities in the IMM model are identical to the corresponding meshes in the conventional model, save for the separation into standalone entity meshes. The resin mesh in the IMM models, while having the same geometry as the corresponding conventional models, will be constructed in the IMM manner described previously. In this way, both of the characteristics of the second and third bullets are present in the IMM models.

This thesis begins with a review of the literature relevant to the modeling and analysis of textile composites. First, the body of work in three dimensional finite element analysis of textile composites is discussed. Second, the existing methods for simulation of textile geometry are presented, as well as some meshing related efforts. A theory section then describes the finite element formulations relevant to both the conventional and IMM approaches used herein. Next, the analysis configurations used in evaluation of the IMM are detailed. The first configuration is a plain weave textile unit cell as the chosen textile composite model for evaluation. The second configuration discussed is a simplified two-inclusion model upon which all character-

istics of the IMM can be implemented in a manner where their impacts are more readily observable than with the textile. Results of the two analysis configurations are then presented. An investigation into the behavior of the penalty method under various refinements and weights is given in the context of the two-inclusion configuration. Solution convergences, as well as comparisons of the predicted stress fields, are presented for both configurations using suitable refinements and penalty weight. Lastly, a summary of the results, the conclusions drawn, and the direction of future work is provided.

In an effort to more accurately model and analyze the behavior of textile composites, new techniques are being developed. This work hopes to establish an understanding of one such new technique, to provide a foundation for it to be used in analysis of complex textile architectures upon which other analysis methods can not be readily used.

2. LITERATURE REVIEW

Mesoscale modeling is central to the analysis of textile composites. As such, there is significant literature regarding analysis methods. This chapter presents a cursory review of previous work and state of the art in mesoscale finite element analysis of textile composite unit cells, as well as the methods by which the geometry in those models was produced. First, the significant contributions to the finite element analysis are discussed. Second, the body of work pertaining to the creation or simulation of textile geometry is presented.

2.1 Finite Element Analysis of Textile Composites

The works presented in this section focus on analyses intended to investigate the distribution of local stresses within the unit cell for purposes of understanding how the geometry affects stress distributions and ultimately damage. Many analytic methods, and many finite element analyses, have been developed for mesoscale models with the sole purpose of stiffness prediction; these types of methods are not discussed. The works presented first cover conventional finite element techniques which use conventional element formulations and compatible meshes, and then non-conventional methods.

2.1.1 Conventional finite element work

Perhaps the first finite element analysis of a textile composite, geared toward stress analysis, was accomplished by Whitcomb in [2]. In this work, three dimensional finite element analysis is performed on a plain woven composite unit cell. The unit cell was modeled using idealized geometry and meshed with linear elastic elements. Several different plain woven geometries were analyzed to determine the

effect of tow waviness on the effective material properties and internal stress and strain distributions. It was shown that tow waviness and predicted effective moduli were directly related. Although this work was limited to linear elastic analysis, such that damage propagation could not be investigated, the work defines the basis for three dimensional stress analysis of a textile unit cell. In a later work, Whitcomb and Tang extend the study of the effect of waviness on effective stiffnesses to satin and twill woven composites [8].

Blackketter et al. developed a three dimensional finite element model for the plain weave composite for damage analysis in [9]. Effective constitutive properties for the tows were evaluated using a lower scale micro-mechanical model of fibers and matrix. The unit cell was modeled using idealized geometry, and damage was modeled using a non-linear stiffness reduction scheme developed by the authors. In the analyses, both tension and shear loadings were investigated, and results compared well with experimental data. It was shown that non-linear behavior under shear was principally due to damage propagation rather than plasticity in the matrix.

Chapman and Whitcomb investigated the effects of geometric approximations on plain weaves in [3]. In this work the textile was modeled using idealized geometry with lenticular shaped tow cross sections, full contact between tows, and sinusoidal tow paths. The focus of the investigation was the effects of modeling the tow geometry by sweeping the tow cross section along the tow path, or simply translating it. When a constant cross section is swept, it remains orthogonal to the tow path, and when it is translated the constant cross section remains vertical, i.e. it does not rotate. The difference in geometry is subtle at low tow waviness (the amplitude of the sinusoidal tow path) and is amplified at high waviness. A translated constant cross section distorts the volume of the tow at high waviness. The results of the stress analysis for the two geometric representations follow the same trend.

Whitcomb and Srirengan carried the studies of geometric approximations and mesh characteristics into failure analysis of plain weave composites in [10]. Several model characteristics were studied including quadrature order, mesh refinement, the chosen damage model, and tow waviness. Notably, the predicted strength was observed to decrease significantly as tow waviness increased. Tow waviness was also shown to affect the stress at which damage initiates, and the stress component responsible for furthering damage was shown to change as damage progressed.

Thom supplemented the investigation into the effects of certain geometric and mesh related approximations on the stress analysis of plain weave composites in [11]. While Chapman and Whitcomb explored the effects of tow waviness and the methods by which the tow volume is geometrically constructed from the tow cross section, Thom evaluated the influence of mesh refinement, the size of the unit cell volume occupied by pure matrix, the shape function of the tow path, and linear versus non-linear analysis. Thom concludes that the best way to model gaps in the fabric, within a single ply, is to model the tow cross section with a blunt edge. This allows pockets of pure resin to be modeled between the tows without the need for a step in tow curvature, or for out of plane separation between the tows, as done by Dasgupta et al. in [12], which eliminates the tow-to-tow contact. The proposed elliptical tow path, as opposed to sinusoidal, is observed to have strong influence on the stiffness and peak stress distributions. Linear analysis is determined sufficient for laminates.

Carvelli and Poggi developed a two step homogenization procedure to predict both the stiffness and strength of woven fabric laminates in [13]. A fiber matrix representative volume element (RVE) is first analyzed to predict effective mechanical properties for tows, given a specified fiber volume fraction. The fibers in the fiber matrix RVE are modeled assuming periodic hexagonal packing. The effective tow

properties were then used to model a 3 harness satin unit cell in a three dimensional finite element damage model. The goal of the work was to develop the framework in a manner suitable for implementation in commercially available finite element software.

Whitcomb et al. developed methods for obtaining boundary conditions for periodic analysis of textile composites and for reducing domain size by exploiting material symmetries in [8]. Periodic boundary conditions are developed for a 1/32 region of a symmetrically stacked plain weave unit cell and for a 1/2 region of a simply stacked 8-harness satin weave unit cell. These techniques are generalized by Tang and Whitcomb in [14].

Goyal and Whitcomb analyzed the effects of braid angle, waviness, material properties, and cross sectional shapes in 2 x 2 biaxial braided composites in [15, 16]. In these analyses it was shown that braided fabrics see higher stress concentrations than other comparable fabrics. Stress concentrations were observed to be highly influenced by braid angle, and increased nearly linearly with waviness.

2.1.2 Non-conventional finite element work

One of the limiting factors of all of the above mentioned work is the approximation of geometry by idealization. As mentioned previously, even after this approximation, creating a suitable finite element mesh still presents a difficult task. And as less geometric idealizations are made the task of meshing becomes harder. This theme has been addressed in the literature in several ways. One is to develop new algorithms for producing conventional finite element meshes, sometimes referred to as conformal, for models with complex geometry. Another is to adapt the finite element formulation to use non-conventional element formulations, or a non-conformal mesh. Either way, the issue being addressed is the same: generating a suitably detailed finite element

mesh for textile composites is challenging.

Woo and Whitcomb implemented a Global/Local finite element method for textile composites using macro finite elements [17, 18]. This method was developed to address issues in computing time and resources by removing the need for a highly detailed finite element mesh for the entire domain. By the use of the so called macro finite elements, a relatively coarse (global) mesh could be constructed for a large domain using homogenized material properties, with subdomain (local) meshes constructed for regions of interest to enhance the information at the global level. The subdomain meshes would discretely model the heterogeneous constituents within the domain. Results from the global analysis, namely displacements at nodes along the global/local boundary, were used to define the boundary conditions on the subdomain analyses. The results of the subdomain analyses would then be used to influence the forces at the global level. Although this method is proven effective at reducing computation time and resources, the stress-strain distributions were shown to contain significant error near the global/local boundary.

Cox et al. developed the Binary Model for textile composites to circumvent the need for generating complex meshes [19, 20]. In this model, one dimensional elements are used to represent tow axial stiffness, and are arranged to follow a tow's path in a piecewise linear fashion. The one dimensional line elements are then fixed within three dimensional elements through the use of multipoint constraints. The three dimensional elements represent what the authors term the *effective medium* that is dominated by the matrix constitutive properties. Because of this approximation, the model is capable of predicting effective stiffnesses but lacks sufficient information for predicting failure. To this end, the author's supplemented the model with a specialized strain averaging technique and a method for predicting strength [21, 22].

Belytschko et al. developed what is known as the Structured Extended Finite

Element Method (XFEM) as a means for modeling geometrically complex solids without the need for constructing a mesh that conforms to the geometry. Although not developed explicitly for textile composites, XFEM has found applications in the field. Within the XFEM framework, characteristics such as material interfaces or cracks are defined as implicit surfaces within elements, and represented using radial basis functions. Because of this, the entire domain can be meshed using a structured mesh, while the geometric complexities are transferred to the model by the implicit surfaces defined by mathematical equations. The XFEM formulation is sufficiently complex on its own and will not be discussed in detail herein.

Jiang et al. developed the Domain Superposition Technique (DST) for modeling textile composites [23]. In DST, the volumes of tows and matrix are meshed separately, while the matrix occupies the entire volume of the textile unit cell, and then the two meshes are superimposed to produce a combined model. The matrix mesh is structured and has no need to conform elements to the tow-matrix material interfaces. The elements of the matrix mesh are assigned material properties corresponding to the actual matrix, and the elements of the tow mesh are assigned material properties based on the difference between the matrix and tow properties. Continuity between the matrix and tow meshes is handled using a constraint coupling technique which requires the nodal displacements of the tow meshes to be equal to that of the global matrix mesh. This method does not make use of an iterative procedure, as opposed to the mesh superposition techniques developed by Fish et al. [24], which have been adapted for use in textile composites.

Kumar et al. developed a method for performing finite element analysis using a nonconforming mesh [25, 26]. In this method, the entire analysis domain, regardless of internal and external geometry, is meshed using a structured grid. Any external or internal geometric features are represented using implicit surfaces defined by math-

ematical equations, which take the form of approximate step functions and are used to evaluate the volume integrals. This method has many characteristics of XFEM, but uses a specialized method for imposing boundary conditions which the authors refer to as the Implicit Boundary Method (IBM).

Tabatabaei et al. proposed an alternative method for meshing textile composites which they refer to as the Embedded Element (EE) technique [27, 28]. In the EE technique, the matrix and tows are meshed separately, with the matrix volume covering the entire domain, and then the tow mesh is embedded within the matrix mesh. The degrees of freedom of the embedded mesh (the tow mesh) become slave to interpolated values of corresponding degrees of freedom of the host mesh (the matrix mesh). A description of the constitutive model for the overlapping region is not supplied. The EE is geared toward implementation in commercial finite element software.

2.2 Simulation of Textile Geometry

Much of the work done in textile geometry simulation is accomplished in tandem with stress analysis, but this review will focus on the production of geometric descriptions for purposes of finite element meshing. The methods of geometry simulation fall into three camps: either the geometric architecture is solely based on geometric data, the architecture is enhanced using image based analysis, or it is produced through physics based simulation. Work belonging to each camp will be discussed.

2.2.1 Geometric based description

Peirce proposed the first significant model of fabric geometry where tow (yarn or thread) cross sections were circular [29]. In this model, tow paths were represented in a series of straight lines and circular arcs. Thus the straight lines represent the undulating portion of the tow path, and the circular arc represents the cross over region,

where the tow path arcs around the cross section of the adjacent tow maintaining full tow-to-tow contact. The linear region of the tow path is the most significant limitation of this model, because in reality the bending stiffness of the fibers would not lead to such a linear path.

Kemp further developed the Peirce geometry with the proposition of the racetrack tow cross section in [30]. This cross section takes the form of two circular arcs attached to the opposing ends of a rectangular cross section. A fabric which maintains tow-to-tow contact in the crossover regions would therefore have a linear section of the tow path as it crosses over an adjacent tow. The tow path therein is still a combination of linear sections and circular arcs. While the racetrack cross section is certainly more representative of the true flattened cross sectional shape of tows, it is still not very accurate.

Hearle and Shanahon proposed a new lenticular tow cross sectional shape in [31, 32]. The lenticular cross section is created by two opposing circular arcs with an offset between their center points. When the center points are coincident, the cross section is circular. A fabric maintaining full tow-to-tow contact in cross over regions will have its tow path predominantly defined by the cross section itself. When there are no linear regions in the tow path, the cross section completely defines the tow path. This cross sectional representation is widely accepted as a sufficient description of the flattened fabric geometry.

Hivet and Boisse developed an automated CAD geometry based simulation of fabrics [33]. In this framework, the cross sections of tows are formed using four customizable line segments. Each line segment can take the form of a straight line or parabola. Tow paths are driven by the cross sections of adjacent tows to maintain tow-to-tow contact. When more than two tows are in contact, straight line segments are used to simplify the tow cross section. Tow paths in contact free zones are straight

in light of minimal bending stiffness. In this way, tow cross sections vary along the length of the tow. The method was implemented for two dimensional fabrics e.g. plain, satin, and twill woven fabrics.

The works of Robitaille et al. [34, 35, 36, 37] formed the basis for the textile geometry simulation and finite element meshing software TexGen. TexGen is an integrated textile modeling and analysis software package built upon a generalized textile geometry construction methodology. TexGen is capable of modeling two dimensional and three dimensional textile architectures. In TexGen, all geometries for all types of textile reinforcements are simulated using a series of vectors representing the tow centerlines. Tow paths are constructed from the vectors by adjoining vector endpoints using circular arcs with first order continuity for smoothing. Tow cross sections, either elliptical or lenticular, are then swept along the tow paths to create solid bodies. In later versions, this smoothing process using vectors and circular arcs was replaced with a series of control points defining the tow path and the use of Bezier and Cubic interpolations for smoothing. TexGen uses input data obtained from observations of real textiles to influence the tow paths, which are otherwise arbitrarily placed. Tow cross sections are tailorable to remove interpenetrations and do not necessarily remain constant along the tow length.

2.2.2 Image enhanced geometric description

Kim and Swan suggested a voxel based meshing method in [38]. This technique uses three dimensional pixels, or voxels, obtained from image processing combined with an adaptive, automated meshing technique [39] to produce locally refined meshes which describe the complex three dimensional textile architecture. Using only the voxel based methodology, a structured hexahedral mesh is created that covers the entire textile unit cell domain. Each voxel (easily convertible to a hexahedral

element) is assigned a material or mixture of material depending on where it lies in mathematically defined sub-domains which describe the shape of the tows and matrix. The voxels which are assigned multiple materials are ultimately handled by being prescribed a material property set that is based on a rule of mixtures. The adaptive, automated refinement technique was therefore developed to refine these mixed material voxels into tetrahedral elements with a single material property. While these models produce accurate estimates of elastic stiffnesses, the characterization of material interface regions are limited due to the shape of voxels and the subsequent artificial tetrahedral refinement. This limitation impedes accurate damage modeling.

Potter et al. describe a further developed voxel based meshing method which better captures the definition of material interfaces in [40]. The material interfaces are improved by using a voxel smoothing technique borrowed from the biomedical field [41]. The developed framework is capable of producing smooth surface hexahedral meshes, directly from the initial voxel description which contains "jagged" material interfaces by nature. Support for the application of periodic boundary conditions is available, and the meshing algorithm contains generality for handling architectural deformity within the textile.

2.2.3 Physics based simulation

Sherburn et al. proposed an energy minimization technique for predicting textile geometry in [42]. In the proposed method, a representation of geometry is initially obtained (namely, from the authors' modeling software TexGen) and then augmented using a finite element based numerical procedure. The initial geometric representation is fitted with plate elements along tow midsurfaces, capturing the tow bending and tensile properties. Contacts between materials are modeling using a penalty

function weighted proportionally to interpenetration distance. Displacements of the tows are captured when solving for the minimum energy configuration and then used to modify the initial geometric representation. The resulting geometry is shown to compare more accurately to textile micrographs than the original.

Lomov et al. have developed a textile modeling and analysis software called WiseTex [43, 44, 45, 46, 47, 48]. Like TexGen, WiseTex is an integrated geometric modeling and analysis software package that supports many types of two dimensional and three dimensional textile architectures. WiseTex uses a combination of several analytic models, educated by physical properties of the fabric, to calculate the textile geometry in its relaxed state. In this way, the software starts with a general description of a textile containing the weave pattern and initial tow cross sectional shapes, and then employs an analytic energy minimization procedure to calculate the relaxed configuration. This process requires input data describing the physical properties of the fabric determined experimentally. For example, Desplentere et al. studied variability in micro-ct scans of 3d warp knitted textile composites to build geometric data sets for input into WiseTex in [49].

Perhaps the most general method for simulating the geometry of textile composites is the mechanical based simulation of the multi-chain digital element technique [6, 5]. This method attempts to reproduce the entire weaving and relaxation process by directly modeling the mechanical behavior of fibers, represented by multi-chain digital elements, and bundles of fibers woven together in a specified pattern and placed under tension. Due to computational expenses, tows are modeled as a bundle of an arbitrary number of fibers, or multi-chain digital elements, usually between 15 and 80. The relaxation process is an iterative procedure that applies tension to the ends of each fiber, calculates a displacement, and then the resulting interaction with the other fibers. Multi-chain digital elements are essentially a series of spherical ele-

ments along a string; when these elements come into contact with eachother, contact forces are generated to cause a reaction. After the fabric is sufficiently relaxed, geometric calculations can be performed to form solid boundaries encasing each bundle of fibers to form tow volumes. This modeling process is general and can be applied to a number of different weave patterns, tow diameters, and spacings. Resulting geometries closely resemble observed fabrics. Limitations of this methodology are related to finite element meshing of the produced geometry, as discussed throughout this thesis.

Drach et al. developed a finite element meshing framework in [50] for the purposes of creating high quality, conformal finite element meshes for geometry produced by an implementation of the multi-chain digital element technique [6] in DEA Fabric Mechanics Analyzer (DFMA). It is important to note that the present thesis is focused on the IMM, which was developed for obtaining, and utilizing, non-conformal finite element meshes for geometry produced by a separate implementation of the multi-chain digital element technique in VTMS.

Grail et al. attacked the problem of generating conforming finite element meshes for complex geometries in [51]. Geometric models of textiles that result from modeling compaction and relaxation often contain complexities, such as interpenetrations, that make traditional finite element meshing very difficult. These complexities can be dealt with by adjusting the cross sections of tows such that they are not in contact, but this introduces artificial matrix layers. The authors describe algorithms for ensuring mesh compatibility between tows that have come into contact with eachother. In practice, when geometric descriptions of two tows in contact are meshed, the resulting mesh contains interpenetrations. This is due to the reduction in geometric fidelity when fitting finite elements to the boundaries. The algorithms described therein are capable of removing these interpenetrations, while maintaining smooth

tow surfaces, and producing conformal tow surface meshes.

To date, there has been substantial work in the modeling and analysis of textile composites. While conventional approaches which make use of idealized geometries are well established, novel approaches for simulating more realistic geometric descriptions are just emerging. These newer approaches come along with modifications to the finite element formulations which are used to analyze them. Little to no work has been done to evaluate the significance of these more realistic textile geometries.

3. THEORY

This chapter details the theory behind the tools used to perform the analyses in this work. The conventional formulation of elastic finite elements in three dimensions is presented first. Then the IMM adaptations are discussed.

3.1 Conventional Finite Element Formulation

This section develops what is referred to herein as conventional finite element analysis, which is an implementation of the three-dimensional elastic finite element method. Finite element analysis is based on the discretization of the analysis domain into elements, or a mesh. These elements are assigned various constitutive properties corresponding to the material which occupies its volume. Element stiffnesses are developed from these constitutive properties to satisfy the governing equilibrium equations. Boundary conditions are formed through the specification of either force or displacement over the entire boundary of the mesh. These boundary conditions, together with the element stiffnesses, are used to form a system of linear equations for equilibrium. The solution of this system is the collection of nodal forces and displacements for equilibrium. Through the use of kinematic relationships, full field strains can be calculated from these displacements. Stresses are then obtained using the constitutive relationships. The following sections discuss these operations in detail.

3.1.1 Kinematic relationships

3.1.1.1 Spatial description

There are two reference frames for describing the deformation of a material. The Lagrangian, known as the material description, is formed in terms of the undeformed

configuration where a material point is denoted by reference coordinates X_i. The second reference frame, the Eulerian frame, known as the spatial description, is formed in terms of the deformed configuration where material points are defined by the spatial coordinates x_i. A mapping function exists relating a point in the deformed material x_i to its reference point X_i and is shown in Equation 3.1.

$$x_i = \chi(X_i, t) \tag{3.1}$$

In the case where $t = t_o$, the above equation results in $x_i = X_i = \chi(X_i, t_o)$.

3.1.1.2 Displacement

Given Equation 3.1, which provides the Eulerian description in terms of the Lagrangian, it is straightforward to form an expression for displacement. The definition of displacement in Equation 3.2 is the change in position of a material point from its reference configuration to its deformed configuration, and is written entirely in terms of the Lagrangian description with the assistance of Equation 3.1.

$$u_i = x_i - X_i \tag{3.2}$$

3.1.1.3 Infinitesimal strain

The deformation gradient, F, is defined in Equation 3.3 where the Kronecker delta δ_{ij} is used for simplicity.

$$F_{ij} = \frac{\partial x_i}{\partial X_j} = \frac{\partial \chi(X_i, t)}{\partial X_j} = \frac{\partial u_i}{\partial X_j} + \delta_{ij} \tag{3.3}$$

From the deformation gradient the right stretch tensor, C, also known as the

right Cauchy-Green deformation tensor, is computed as in Equation 3.4.

$$C_{ij} = F_{ki}F_{kj} \tag{3.4}$$

The Green-Lagrange strain tensor is defined as, and obtained using, Equation 3.5.

$$\begin{aligned} E_{ij} &= \frac{1}{2}(C_{ij} - \delta_{ij}) \\ &= \frac{1}{2}\left(\frac{\partial u_i}{\partial X_j} + \frac{\partial u_j}{\partial X_i} + \frac{\partial u_k}{\partial X_i}\frac{\partial u_k}{\partial X_j}\right) \end{aligned} \tag{3.5}$$

Lastly the linearized infinitesimal strain tensor, ε, is derived assuming that the second order term in Equation 3.5 is negligible given the linearizing assumption, and that $\frac{\partial u_i}{\partial X_j} \approx \frac{\partial u_i}{\partial x_j}$ given that strains are small. This results in Equation 3.6.

$$\begin{aligned} \varepsilon_{ij} &= \frac{1}{2}\left(\frac{\partial u_i}{\partial X_j} + \frac{\partial u_j}{\partial X_i}\right) \\ &\approx \frac{1}{2}\left(\frac{\partial u_i}{\partial x_j} + \frac{\partial u_j}{\partial x_i}\right) \end{aligned} \tag{3.6}$$

Given this description, the difference between the Eulerian and Langrange descriptions becomes negligible, and all spatial coordinates can be given in the form x_i. The infinitesimal strain tensor is also shown to be symmetric by definition since it contains the addition of a matrix and its transpose.

3.1.2 Constitutive relationships

The constitutive rule provides a relationship between stress and strain, and ultimately between loads and deformation. The linear elastic constitutive model is based on Hooke's law, which proposes a linear relationship between stress and strain described by a fourth order tensor C_{ijkl}, known as the stiffness tensor. The stress

strain relationship, in the absence of thermal strains, is shown in Equation 3.7.

$$\sigma_{ij} = C_{ijkl}\varepsilon_{kl} \tag{3.7}$$

The fourth order tensor, C_{ijkl}, is Cartesian based such that it contains 81 unique entries, or independent constants. However, due to the noted symmetry in the strain tensor, as well as similar symmetry in the stress tensor required for equilibrium of angular momentum, the number of unique entries can be reduced by the relations $C_{ijkl} = C_{jikl} = C_{ijlk}$. This is known as the minor symmetry and results in the following matrix-expanded relationship.

$$\begin{bmatrix} \sigma_1 \\ \sigma_2 \\ \sigma_3 \\ \sigma_4 \\ \sigma_5 \\ \sigma_6 \end{bmatrix} = \begin{bmatrix} C_{11} & C_{12} & C_{13} & C_{14} & C_{15} & C_{16} \\ C_{21} & C_{22} & C_{23} & C_{24} & C_{25} & C_{26} \\ C_{31} & C_{32} & C_{33} & C_{34} & C_{35} & C_{36} \\ C_{41} & C_{42} & C_{43} & C_{44} & C_{45} & C_{46} \\ C_{51} & C_{52} & C_{53} & C_{54} & C_{55} & C_{56} \\ C_{61} & C_{62} & C_{63} & C_{64} & C_{65} & C_{66} \end{bmatrix} \cdot \begin{bmatrix} \varepsilon_1 \\ \varepsilon_2 \\ \varepsilon_3 \\ \varepsilon_4 \\ \varepsilon_5 \\ \varepsilon_6 \end{bmatrix} \tag{3.8}$$

Equation 3.8 uses contracted notation such that the subscripts (1, 2, 3, 4, 5, 6) correspond to the expanded subscripts (11, 22, 33, 23, 31, 12). Also, the shearing strains equal twice their tensorial values. A further reduction in independent constants can be made through the major symmetry of the stiffness matrix observed through the strain energy function, Equation 3.9, which should be insensitive to the order of ij and kl indices.

$$U = C_{ijkl}\varepsilon_{ij}\varepsilon_{kl} = C_{klij}\varepsilon_{ij}\varepsilon_{kl} \tag{3.9}$$

With the major symmetry stating that $C_{ijkl} = C_{klij}$, the constitutive relationship shown in Equation 3.8 simplifies to Equation 3.10, where there remain 21 nonzero independent constants.

$$\begin{bmatrix} \sigma_1 \\ \sigma_2 \\ \sigma_3 \\ \sigma_4 \\ \sigma_5 \\ \sigma_6 \end{bmatrix} = \begin{bmatrix} C_{11} & C_{12} & C_{13} & C_{14} & C_{15} & C_{16} \\ C_{12} & C_{22} & C_{23} & C_{24} & C_{25} & C_{26} \\ C_{13} & C_{23} & C_{33} & C_{34} & C_{35} & C_{36} \\ C_{14} & C_{24} & C_{34} & C_{44} & C_{45} & C_{46} \\ C_{15} & C_{25} & C_{35} & C_{45} & C_{55} & C_{56} \\ C_{16} & C_{26} & C_{36} & C_{46} & C_{56} & C_{66} \end{bmatrix} \cdot \begin{bmatrix} \varepsilon_1 \\ \varepsilon_2 \\ \varepsilon_3 \\ \varepsilon_4 \\ \varepsilon_5 \\ \varepsilon_6 \end{bmatrix} \tag{3.10}$$

This is the general stiffness tensor for an anisotropic material, and can be simplified further by appealing to a particular material symmetry. This is done by transforming the stiffness tensor according to the material symmetries, and imposing invariance. The analysis tools used in this thesis make use of material files capable of describing a material with orthotropic symmetry. An orthotropic material has three orthogonal plains of symmetry and after simplification its stiffness tensor contains 12 nonzero entries with only 9 independent constants. These constants are most conveniently described through the compliance tensor, S, which is the inverse of the stiffness tensor. The compliance tensor for an orthotropic material is shown in Equation 3.11, relating strain to stress using engineering properties. Recall the major symmetry of the stiffness tensor such that the relations $\frac{\nu_{12}}{E_1} = \frac{\nu_{21}}{E_2}$, $\frac{\nu_{13}}{E_1} = \frac{\nu_{31}}{E_3}$, and $\frac{\nu_{23}}{E_2} = \frac{\nu_{32}}{E_3}$ exist, meaning that only 9 of the 12 total engineering constants are

independent.

$$\begin{bmatrix} \varepsilon_{11} \\ \varepsilon_{22} \\ \varepsilon_{33} \\ 2\varepsilon_{23} \\ 2\varepsilon_{31} \\ 2\varepsilon_{12} \end{bmatrix} = \begin{bmatrix} \frac{1}{E_1} & -\frac{\nu_{21}}{E_2} & -\frac{\nu_{31}}{E_3} & 0 & 0 & 0 \\ -\frac{\nu_{12}}{E_1} & \frac{1}{E_2} & -\frac{\nu_{32}}{E_3} & 0 & 0 & 0 \\ -\frac{\nu_{13}}{E_1} & -\frac{\nu_{23}}{E_2} & \frac{1}{E_3} & 0 & 0 & 0 \\ 0 & 0 & 0 & \frac{1}{G_{23}} & 0 & 0 \\ 0 & 0 & 0 & 0 & \frac{1}{G_{31}} & 0 \\ 0 & 0 & 0 & 0 & 0 & \frac{1}{G_{12}} \end{bmatrix} \cdot \begin{bmatrix} \sigma_{11} \\ \sigma_{22} \\ \sigma_{33} \\ \sigma_{23} \\ \sigma_{31} \\ \sigma_{12} \end{bmatrix} \tag{3.11}$$

The meanings of the engineering constants used in Equation 3.11 are as follows: the E_i are the Young's moduli in the i directions, the G_{ij} are the shear moduli in the ij planes, and the ν_{ij} are the Poisson ratios for transverse strain in the j direction when stressed in the i direction. In this work, materials will either be assigned transversely isotropic material properties, or isotropic material properties. Transverse isotropy is a material symmetry that, in addition to orthotropic symmetry, contains a rotational symmetry about one axis, usually the first. The transverse isotropic stiffness matrix contains 12 nonzero entries that can be characterized using 5 independent constants. Isotropy is a material symmetry that, in addition to transverse isotropy, contains rotational symmetry about the remaining two axes. The isotropic stiffness matrix contains 12 nonzero entries that can be characterized using only 2 independent constants.

3.1.3 Weak form derivation for elasticity

The finite element formulation for elasticity begins with the equation for equilibrium of a deformable body given by Equation 3.12.

$$\frac{\partial \sigma_{ij}}{\partial x_j} + f_i = 0 \tag{3.12}$$

Following the principle of virtual work, Equation 3.12 is then multiplied by virtual displacements, δu_i, and then integrated over the domain V to produce the weighted residual.

$$\int_V \delta u_i \left(\frac{\partial \sigma_{ij}}{\partial x_j} + f_i \right) dV = \int_V \left(\delta u_i \frac{\partial \sigma_{ij}}{\partial x_j} + \delta u_i f_i \right) dV = 0 \tag{3.13}$$

Integrating the first term in Equation 3.13 by parts results in Equation 3.14.

$$\int_V \left(\frac{\partial (\delta u_i \sigma_{ij})}{\partial x_j} - \sigma_{ij} \frac{\partial \delta u_i}{\partial x_j} + \delta u_i f_i \right) dV = 0 \tag{3.14}$$

The divergence theorem can then be applied to the first term in Equation 3.14 to result in Equation 3.15 where S represents the boundary of the volume V.

$$\int_S (\delta u_i \sigma_{ij} n_j) \, dA + \int_V \left(\delta u_i f_i - \sigma_{ij} \frac{\partial \delta u_i}{\partial x_j} \right) = 0 \tag{3.15}$$

Now, Cauchy's stress formula which relate stress to tractions, T, at the boundary is given by Equation 3.16. In addition, the implication of symmetry in the stress tensor, as well as Equation 3.6, allow for the following product to be rewritten as in Equation 3.17.

$$T_i = \sigma_{ij} n_j \tag{3.16}$$

$$\frac{\partial \delta u_i}{\partial x_j} \sigma_{ij} = \delta \varepsilon_{ij} \sigma_{ij} \tag{3.17}$$

Equation 3.16 together with Equation 3.17 can be substituted into Equation 3.15 to yield the following final weak form.

$$\int_S (\delta u_i T_i) \, dS + \int_V (\delta u_i f_i - \sigma_{ij} \delta \varepsilon_{ij}) \, dV = 0 \tag{3.18}$$

3.1.4 Finite element model

The displacements within a finite element u_i, which are governed by Equation 3.18, are approximated by a sum of interpolation functions multiplied by nodal displacements. Within an element containing n nodes, each node has an associated interpolation function ψ^m, where the superscript m denotes the node. The interpolation functions are formed such that ψ^m has the value 1 at the m^{th} node, and 0 at all other nodes in the element. This leads to the approximations for displacement and virtual displacement given by Equations 3.19 and 3.20.

$$u_i = \sum_{m=1}^{n} u_i^m \psi^m \tag{3.19}$$

$$\delta u_i = \sum_{m=1}^{n} \delta u_i^m \psi^m \tag{3.20}$$

In the above expressions the u_i^m denotes the nodal displacements at node m. It is convenient to form the vector q containing all components of all nodal displacements, or degrees of freedom, in a given element.

$$q = \left[\begin{array}{cccccccccccc} u_1^1, & u_2^1, & u_3^1, & \ldots, & u_1^m, & u_2^m, & u_3^m, & \ldots, & u_1^n, & u_2^n, & u_3^n \end{array} \right] \tag{3.21}$$

With this vector, q, the virtual displacement, Equation 3.20, and the virtual strain, Equation 3.17, can be written as the following.

$$\delta u_i = \frac{\partial u_i}{\partial q_\alpha} \delta q_\alpha \tag{3.22}$$

$$\delta \varepsilon_{ij} = \frac{\partial \varepsilon_{ij}}{\partial q_\alpha} \delta q_\alpha \tag{3.23}$$

Applying the weak form to the element and substituting in the above expressions

produces the following.

$$\int_{S_e} \left(\frac{\partial u_i}{\partial q_\alpha} \delta q_\alpha T_i \right) dS_e + \int_{V_e} \left(\frac{\partial u_i}{\partial q_\alpha} \delta q_\alpha f_i - \sigma_{ij} \frac{\partial \varepsilon_{ij}}{\partial q_\alpha} \delta q_\alpha \right) dV_e = 0 \tag{3.24}$$

In Equation 3.24, the subscript, e, on the integral limits, signifies that the integration is done over a single element. The δq_α can be factored out from the integrals, and it can be observed that since Equation 3.24 must hold true for any arbitrary value of δq_α, the following must be true.

$$\int_{S_e} \left(\frac{\partial u_i}{\partial q_\alpha} T_i \right) dS_e + \int_{V_e} \left(\frac{\partial u_i}{\partial q_\alpha} f_i - \sigma_{ij} \frac{\partial \varepsilon_{ij}}{\partial q_\alpha} \right) dV_e = 0 \tag{3.25}$$

After rearranging,

$$\int_{V_e} \left(\sigma_{ij} \frac{\partial \varepsilon_{ij}}{\partial q_\alpha} \right) dV_e = \int_{S_e} \left(\frac{\partial u_i}{\partial q_\alpha} T_i \right) dS_e + \int_{V_e} \left(\frac{\partial u_i}{\partial q_\alpha} f_i \right) dV_e \tag{3.26}$$

This expression is now rewritten in familiar finite element terms. The left hand side of Equation 3.26 can be simplified by making the use of contracted notation such that,

$$\varepsilon_i = [\varepsilon_{11}, \varepsilon_{22}, \varepsilon_{33}, 2\varepsilon_{23}, 2\varepsilon_{13}, 2\varepsilon_{12}]^T \tag{3.27}$$

$$\sigma_i = [\sigma_{11}, \sigma_{22}, \sigma_{33}, \sigma_{23}, \sigma_{13}, \sigma_{12}]^T \tag{3.28}$$

as well as the introduction of the the strain-displacement matrix, B, which contains

the partials of the interpolation functions used in calculating strains.

$$B = \frac{\partial \varepsilon_k}{\partial q_\alpha} = \begin{bmatrix} \frac{\partial \psi^1}{\partial x_1} & 0 & 0 & \dots & \frac{\partial \psi^n}{\partial x_1} & 0 & 0 \\ 0 & \frac{\partial \psi^1}{\partial x_2} & 0 & \dots & 0 & \frac{\partial \psi^n}{\partial x_2} & 0 \\ 0 & 0 & \frac{\partial \psi^1}{\partial x_3} & \dots & 0 & 0 & \frac{\partial \psi^n}{\partial x_3} \\ \frac{\partial \psi^1}{\partial x_1} & \frac{\partial \psi^1}{\partial x_2} & 0 & \dots & \frac{\partial \psi^n}{\partial x_1} & \frac{\partial \psi^n}{\partial x_2} & 0 \\ \frac{\partial \psi^1}{\partial x_1} & 0 & \frac{\partial \psi^1}{\partial x_3} & \dots & \frac{\partial \psi^n}{\partial x_1} & 0 & \frac{\partial \psi^n}{\partial x_3} \\ 0 & \frac{\partial \psi^1}{\partial x_2} & \frac{\partial \psi^1}{\partial x_3} & \dots & 0 & \frac{\partial \psi^n}{\partial x_2} & \frac{\partial \psi^n}{\partial x_3} \end{bmatrix} \tag{3.29}$$

Incorporating these expressions, the strains and stresses in the left hand side of Equation 3.26 can be rewritten as Equation 3.30 and Equation 3.31 respectively.

$$\varepsilon_k = B_{k\alpha} q_\alpha \tag{3.30}$$

$$\sigma_k = C_{kl} \varepsilon_l = C_{kl} B_{l\beta} q_\beta \tag{3.31}$$

This allows the entire left hand side to take the form Equation 3.32.

$$\int_{V_e} \left(\sigma_{ij} \frac{\partial \varepsilon_{ij}}{\partial q_\alpha} \right) dV_e = \int_{V_e} \left(B_{k\alpha} C_{kl} B_{l\beta} q_\beta \right) dV_e = \int_{V_e} \left(B_{k\alpha} C_{kl} B_{l\beta} \right) dV_e q_\beta = K^e_{\alpha\beta} q_\beta \tag{3.32}$$

Turning to the right hand side of Equation 3.26, it is convenient to group the integrals together into a single force vector, F^e, shown in component and expanded form in Equations 3.33 and 3.34 respectively.

$$F^e_\alpha = \int_{S_e} \left(\frac{\partial u_i}{\partial q_\alpha} T_i \right) dS_e + \int_{V_e} \left(\frac{\partial u_i}{\partial q_\alpha} f_i \right) dV_e \tag{3.33}$$

$$F^e = \begin{bmatrix} \int_{S_e} (T_1\psi^1)\, dS_e + \int_{V_e} (f_1\psi^1)\, dV_e \\ \int_{S_e} (T_2\psi^1)\, dS_e + \int_{V_e} (f_2\psi^1)\, dV_e \\ \int_{S_e} (T_3\psi^1)\, dS_e + \int_{V_e} (f_3\psi^1)\, dV_e \\ \vdots \\ \int_{S_e} (T_1\psi^m)\, dS_e + \int_{V_e} (f_1\psi^m)\, dV_e \\ \int_{S_e} (T_2\psi^m)\, dS_e + \int_{V_e} (f_2\psi^m)\, dV_e \\ \int_{S_e} (T_3\psi^m)\, dS_e + \int_{V_e} (f_3\psi^m)\, dV_e \\ \vdots \\ \int_{S_e} (T_1\psi^n)\, dS_e + \int_{V_e} (f_1\psi^n)\, dV_e \\ \int_{S_e} (T_2\psi^n)\, dS_e + \int_{V_e} (f_2\psi^n)\, dV_e \\ \int_{S_e} (T_3\psi^n)\, dS_e + \int_{V_e} (f_3\psi^n)\, dV_e \end{bmatrix} \tag{3.34}$$

Finally, substituting Equation 3.32 and Equation 3.33 into Equation 3.26, the final form of the finite element formulation can be written in the familiar linear system of equations, where K^e and F^e are the element stiffness and force vectors, respectively.

$$K^e_{ij} q_j = F^e_i \tag{3.35}$$

3.1.5 Element formulation

3.1.5.1 Linear 8 node hexahedron interpolation functions

The approximation for the displacement field within an element is based on the summation of all nodal displacements and corresponding interpolation functions within the element. The interpolation functions are formulated such that they have a value of 1 at their respective node, and are equal to 0 at all other nodes. This type of formulation can be accomplished using polynomials, which in turn allows for numerical integration using quadrature rules.

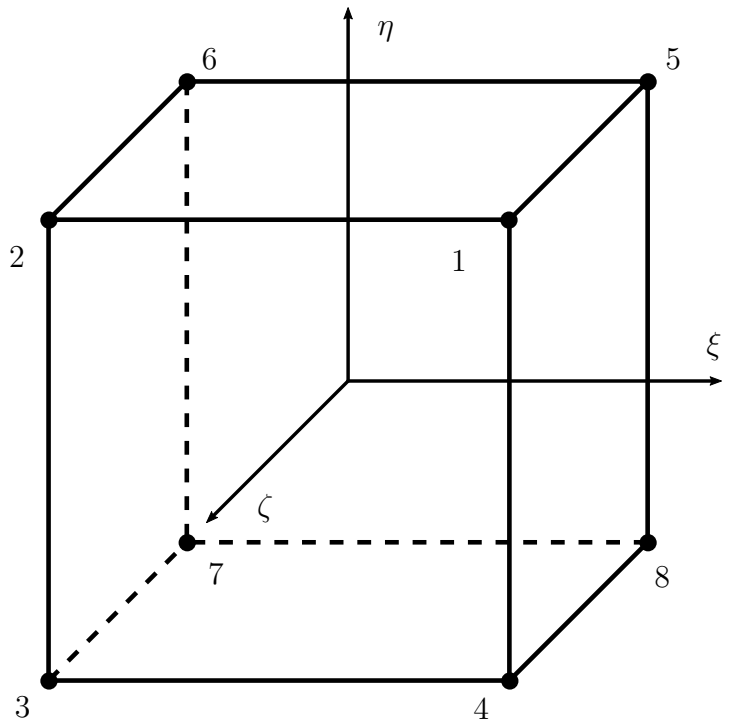

Figure 3.1: 8 node hexahedron master element

In addition, although each element of the physical domain may be unique, the interpolation functions are formulated for a master element that has a domain which ranges from -1 to 1 in its three coordinate directions (ξ, η, ζ), forming a cubic shape. This allows a single set of interpolation functions to be formulated and used for each element given appropriate coordinate transformations which will be discussed in the next section. In addition, the domains over which these shape functions are defined make them suitable for use with numerical integration approaches, discussed later. The analyses in this work primarily make the use of 8 node, linear, hexahedron elements. Figure 3.1 displays the master element for such an element with the nodal connectivity and master coordinate axis labeled.

The interpolation functions for the linear 8 node hexahedron are provided below.

$$\begin{aligned}
\psi^1 &= \frac{1}{8}(1+\xi)(1+\eta)(1+\zeta) \\
\psi^2 &= \frac{1}{8}(1-\xi)(1+\eta)(1+\zeta) \\
\psi^3 &= \frac{1}{8}(1-\xi)(1-\eta)(1+\zeta) \\
\psi^4 &= \frac{1}{8}(1+\xi)(1-\eta)(1+\zeta) \\
\psi^5 &= \frac{1}{8}(1+\xi)(1+\eta)(1-\zeta) \\
\psi^6 &= \frac{1}{8}(1-\xi)(1+\eta)(1-\zeta) \\
\psi^7 &= \frac{1}{8}(1-\xi)(1-\eta)(1-\zeta) \\
\psi^8 &= \frac{1}{8}(1+\xi)(1-\eta)(1-\zeta)
\end{aligned} \tag{3.36}$$

3.1.5.2 Spatial mapping

The integrations required to evaluate the terms in Equation 3.35 are performed using Gaussain quadrature which requires the use of a specific master domain, $\hat{V}_e$. The coordinates of this master element, denoted by (ξ, η, ζ), are mapped to a physical element's coordinates by Equation 3.37.

$$x_i(\xi, \eta, \zeta) = \sum_{m=1}^{n} x_i^m \psi^m \tag{3.37}$$

Where in Equation 3.37, like before, the x_i^m are the components of the coordinates of the m^{th} node. The coordinates $x_i(\xi, \eta, \zeta)$ are the physical coordinates corresponding to the master coordinates (ξ, η, ζ). Although the integration must be performed in the master domain, the partial derivatives required to compute the strain displacement-matrix must be taken with respect to the physical domain. Thus, the derivatives of the interpolation functions must be in respect to the physical

domain, but expressed in terms of the master coordinates. This transformation of derivatives is accomplished through the chain rule as follows.

$$\begin{bmatrix} \frac{\partial \psi^m}{\partial \xi} \\ \frac{\partial \psi^m}{\partial \eta} \\ \frac{\partial \psi^m}{\partial \zeta} \end{bmatrix} = \begin{bmatrix} \frac{\partial x}{\partial \xi} & \frac{\partial y}{\partial \xi} & \frac{\partial z}{\partial \xi} \\ \frac{\partial x}{\partial \eta} & \frac{\partial y}{\partial \eta} & \frac{\partial z}{\partial \eta} \\ \frac{\partial x}{\partial \zeta} & \frac{\partial y}{\partial \zeta} & \frac{\partial z}{\partial \zeta} \end{bmatrix} \begin{bmatrix} \frac{\partial \psi^m}{\partial x} \\ \frac{\partial \psi^m}{\partial y} \\ \frac{\partial \psi^m}{\partial z} \end{bmatrix} = \boldsymbol{J} \begin{bmatrix} \frac{\partial \psi^m}{\partial x} \\ \frac{\partial \psi^m}{\partial y} \\ \frac{\partial \psi^m}{\partial z} \end{bmatrix} \tag{3.38}$$

In Equation 3.38, J denotes the Jacobian, which is computed by taking the required derivatives of Equation 3.37. Note that Equation 3.38 is actually the inverse transformation, and that the partials in the last column are those with respect to the physical coordinates. In order to obtain these in terms of the master coordinates, the Jacobian is first calculated and then inverted to compute the necessary partials as follows.

$$\begin{bmatrix} \frac{\partial \psi^m}{\partial x} \\ \frac{\partial \psi^m}{\partial y} \\ \frac{\partial \psi^m}{\partial z} \end{bmatrix} = \boldsymbol{J}^{-1} \begin{bmatrix} \frac{\partial \psi^m}{\partial \xi} \\ \frac{\partial \psi^m}{\partial \eta} \\ \frac{\partial \psi^m}{\partial \zeta} \end{bmatrix} \tag{3.39}$$

Lastly, the limits of, and domain over which the integrations are performed can be transformed to the master domain using the following equation, where $|\boldsymbol{J}|$ is the determinant of the Jacobian matrix.

$$dV_e = |\boldsymbol{J}| d\hat{V}_e \tag{3.40}$$

With Equations 3.39 and 3.40, the element stiffness and force vector integrations can can be rewritten as follows, where the $B^{'}$ denotes that the contained derivatives have been transformed into the master coordinates using Equation 3.39.

$$K_{ij}^e = \int_{V_e} \left(B_{ki} C_{kl} B_{lj}\right) dV_e = \int_{\hat{V}_e} \left(B_{ki}^{'} C_{kl} B_{lj}^{'}\right) |\boldsymbol{J}| d\hat{V}_e \tag{3.41}$$

$$
\begin{aligned}
F_i^e &= \int_{S_e} \left(\frac{\partial u_j}{\partial q_i} T_j \right) dS_e + \int_{V_e} \left(\frac{\partial u_j}{\partial q_i} f_j \right) dV_e \\
&= \int_{\hat{S}_e} \left(\frac{\partial u_j}{\partial q_i} T_j \right) |\boldsymbol{J}| d\hat{S}_e + \int_{\hat{V}_e} \left(\frac{\partial u_j}{\partial q_i} f_j \right) |\boldsymbol{J}| d\hat{V}_e
\end{aligned}
\tag{3.42}
$$

3.1.5.3 Numerical integration

With the equations written in terms of the master domain, it is possible to proceed with the integrations using Gaussian quadrature. Gaussian quadrature is based on the ability to approximately evaluate the integral of a polynomial function, $f(\xi)$, of order $(2N-1)$ using the summation of values of the polynomial function at N number sample points, ξ_i, times associated weights, w_i.

$$
I = \int_{-1}^{1} f(\xi) d\xi = \sum_{i=1}^{n} w_i f(\xi_i) \tag{3.43}
$$

The sample points, ξ_i, in Equation 3.43, are known as quadrature points. In this work the approximation is repeated in the three dimensions, using the same number of weights in each dimension as in Equation 3.44. The quadrature points and associated weights are provided in Table 3.1.

$$
\begin{aligned}
\int_{\hat{V}_e} f(\boldsymbol{\xi}) d\hat{V}_e &= \int_{-1}^{1} \int_{-1}^{1} \int_{-1}^{1} f(\boldsymbol{\xi}) d\xi_1 d\xi_2 d\xi_3 \\
&= \sum_{i=1}^{N} \sum_{j=1}^{N} \sum_{k=1}^{N} f(\xi_1^i, \xi_2^j, \xi_3^k) W_i W_j W_k
\end{aligned}
\tag{3.44}
$$

3.1.5.4 Solution

After the preceding calculations are performed for each element in the solution domain, the element stiffness matrices and force vectors are combined into global arrays through the process of assembly, which is organized according to degrees of freedom. The resulting equation of the form Equation 3.35 is then solved, using a

Table 3.1: Quadrature point locations and associated weights

Order	Quad Point Locations	Weights
1	0	2
2	$-\sqrt{\frac{1}{3}}, \sqrt{\frac{1}{3}})$	$1, 1$
3	$-\sqrt{\frac{3}{5}}, 0, \sqrt{\frac{3}{5}}$	$\frac{5}{9}, \frac{8}{9}, \frac{5}{9}$

linear systems of equations solver, for the nodal displacements of all nodes in the domain. The approximation for displacement, Equation 3.19, is then used to obtain the full displacement field, and likewise Equation 3.30 can be used to obtain the strain field. Since the error in the full field results is minimized at the location of the quadrature points, the strain is calculated there, and the constitutive expression Equation 3.10 is used to calculate stresses. For the purposes of viewing, these quadrature point stresses are then extrapolated to the nodes of the element, where they are averaged with any adjacent element of the same material containing the same node. In this work, the nodal averaged stresses are what will be viewed and compared. This is because access to the quadrature point stresses calculated for the IMM models is not available, but the averaging techniques used to produce the nodal stresses, which are output, are known.

3.2 Independent Mesh Method Adaptations

Documentation regarding the following characteristics of the IMM only discusses the general procedures involved, with little to no mention of the implementation. Because of this, only the governing principles of the two main characteristics of the IMM will be discussed in this section.

3.2.1 Penalty displacement method

It has been stated earlier that the IMM makes use of separate, standalone meshes for each entity in the model domain. This leads to a need to establish compatibility, or displacement continuity between entities which are intended to be bonded together. In the methods described above, all model entities share a continuous mesh. In this way, even though there may be multiple different constitutive properties assigned to various regions of the mesh (entities), compatibility is maintained through the global assembly process because elements on either side of a material interface share common degrees of freedom. In the case of the IMM, elements on opposing sides of a material interface belong to separate mesh entities, which means that even if they share a face with the exact same spatial distribution of nodes, degrees of freedom are not shared. In most cases for which the IMM was developed, the spatial distribution of nodes on faces of two entities in contact are not identical. In either case, the IMM makes use of a penalty displacement method, based on the minimum-energy variational formulation, to tie the degrees of freedom between boundaries of mesh entities which are in contact.

The penalty term, denoted by δA, is based on the definition of master and background entities, denoted in the following by the symbols $\hat{}$ for master and $\tilde{}$ for background, and is calculated through the following equation.

$$\delta A = \int_{\hat{S}} \alpha \left(\hat{u}_i - \tilde{u}_i\right) \delta \left(\hat{u}_i - \tilde{u}_i\right) d\hat{S} \tag{3.45}$$

Since this integration takes place between the surfaces of the master and background entities, only a small subset of interpolation functions is involved. Furthermore, the integration is performed using the quadrature points on the master surface. In this way, the shape functions belonging to the background surface are evaluated

at the quadrature points belonging to the master surface, and nodal compatibility is not required. The value of the penalty weight, denoted by α in Equation 3.45, is suggested to be obtained by Equation 3.46, where W is a dimensional parameter, and $E11$ is the elastic modulus of the material along the first axis.

$$\alpha = \frac{E11}{W} \tag{3.46}$$

In an IMM analysis, this penalty method for imposing displacement continuity between two mesh entities may be used for any of the following situations:

- Between two compatible meshed surfaces with no interpenetrations. This is the only case in which the penalty method does not have any effect on the stresses, given that the penalty is a sufficient value.
- Between two incompatibly meshed surfaces with no interpenetrations.
- Between two incompatibly meshed surfaces with interpenetrations, without using X3D8 elements. In this case the interpenetrations have been determined to be sufficiently small, and are ignored.
- Between a master surface and an X3D8 element. In this case there is both mesh incomaptibility and interpenetration.

3.2.2 Approximation of resin domain

For all background entities, the displacement field approximation, Equation 3.19, is modified in the following manner. The nodes of each element are checked for coordinates that fall within the volume occupied by a master entity. If an element does not contain any of these nodes, then it is treated normally. If every node of an element is determined to fall within the volume of a master entity, then the

element is discarded. This happens often, as a background entity is initially defined to cover the entire problem domain. The remaining elements which are intersected by the boundary of a master entity are assigned a modified set of quadrature points. These modified quadrature points are placed by fitting tetrahedral elements in the portion of the element which is determined to fall outside of the master volume. The tetrahedral elements are used only for placing quadrature points. The result is referred to by the IMM developers as an X3D8 element.

Figure 3.2 shows a visual representation of the formation of these X3D8 elements for a sample two element configuration. In Figure 3.2a, a background element is intersected by a master element. This particular configuration is shown because this type of intersection is defined by more than one face on the master element, a case in which the IMM algorithm mis-calculates the resulting overlap. In any case where an intersection is defined by more than one face, the intersection is drawn by a single plane connecting points where the boundaries of the background element are intersected by master elements. This is shown in Figure 3.2b, and it results in some integration points which fall inside the master entity. The quadrature points shown in Figure 3.2b are the actual placements made by the IMM. Since some of the quadrature points are placed inside of the overlapping region, some error will be induced on the analysis results for this region.

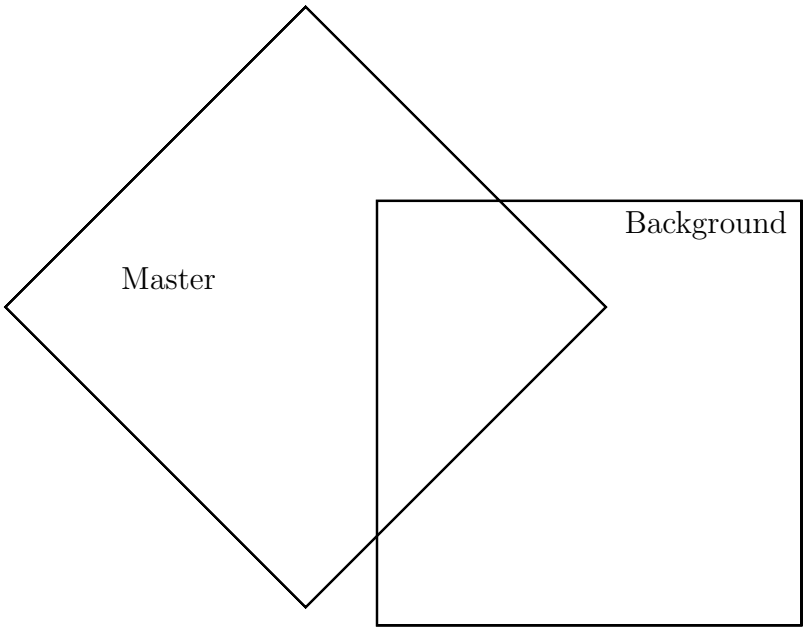

(a) Background element intersected by master element before X3D8 conversion

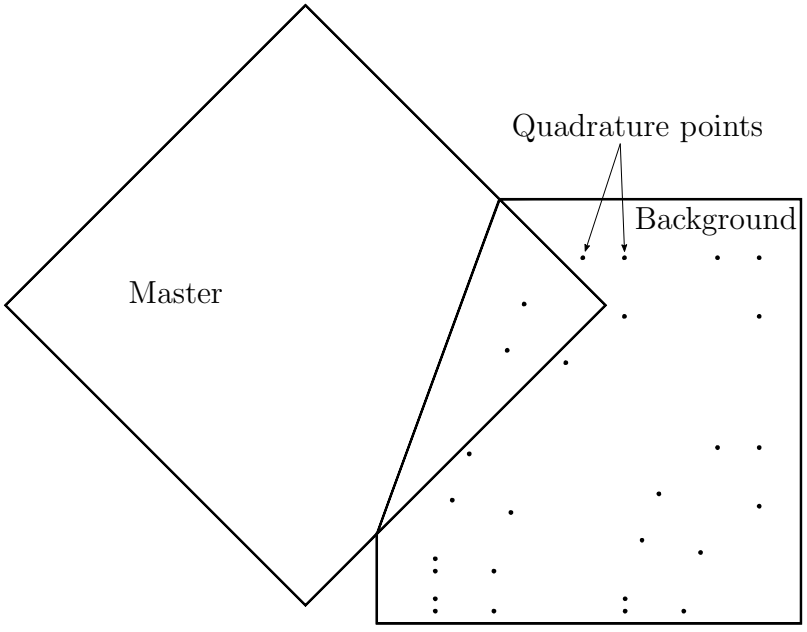

(b) Background element after conversion to X3D8, showing the placement of quadrature points

Figure 3.2: Demonstration of X3D8 element construction showing a known geometric limitation

4. CONFIGURATIONS

The analyses in this work are performed on two configurations. The two configurations make use of the same set of material properties which will be presented at the end of this chapter. First is a symmetrically stacked plain woven textile composite unit cell. The specifics of the geometry and boundary conditions will be discussed in the following section. Second is a simplified two-inclusion model consisting of the cross section of two circular inclusions in close proximity to one another, surrounded by matrix. This configuration was specifically designed to demonstrate the characteristics of the IMM more explicitly than with the plain weave model.

4.1 Plain Weave

4.1.1 Geometry

The chosen plain weave model makes use of idealized geometry, with lenticular tow cross sections and sinusoidal tow paths. Tows remain in full contact through undulation without any gaps between adjacent tows at cross over regions. Because of this, the tow path and tow cross sections are directly related, and the entire geometry can be describe using the waviness ratio, WR, defined in Equation 4.1.

$$WR = \frac{t}{\lambda} \tag{4.1}$$

In Equation 4.1, t designates the thickness of a single ply of the textile, related to the amplitude of the sinusoidal tow path, and λ is the wavelength of the towpath. These parameters are demonstrated on a half width tow cross section in Figure 4.1. It can be seen that in order to maintain tow-to-tow contact, the tow path of an adjacent tow must be equivalent to the boundary of the shown tow's cross section, given that

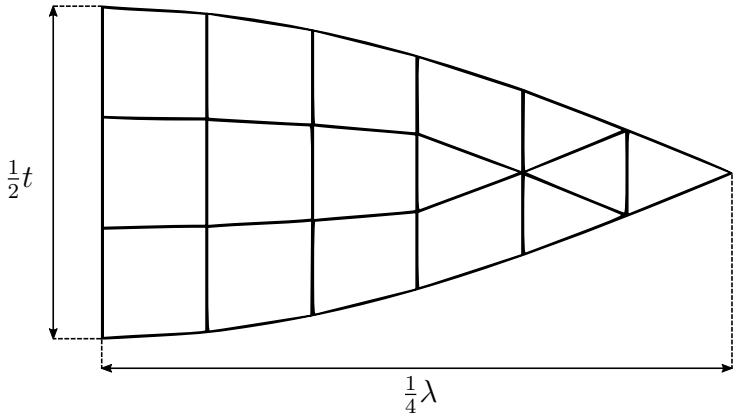

Figure 4.1: Half-width tow cross section

the three dimensional tow volume is created by translating the cross section along the tow path. This, together with sinusoidal tow path form, is how the waviness ratio alone defines the entirety of the weave geometry.

The geometry of the full unit cell for the symmetrically stacked plain weave is shown in Figure 4.2. The geometry shown in Figure 4.2 has a waviness ratio of 1/3, which is relatively high, but is used to amplify the stress gradients. By exploiting material symmetries, with appropriate boundary conditions, the model domain can be reduced to only a portion of the full unit cell with no loss of information [8]. The analyses in this work are performed on a $1/8^{th}$ portion of the full unit cell shown in Figure 4.3.

4.1.2 Mesh

The compatible mesh was generated using a prescribed mesh which translates a tow cross section along the tow path. Since the conventional analysis does not require the use of only linear 8 node hexahedron elements, the compatible matrix mesh contains mixed wedge and hexahedron elements; however, since the compatible meshes for the tows are intended to be used in the IMM model, the tows contain

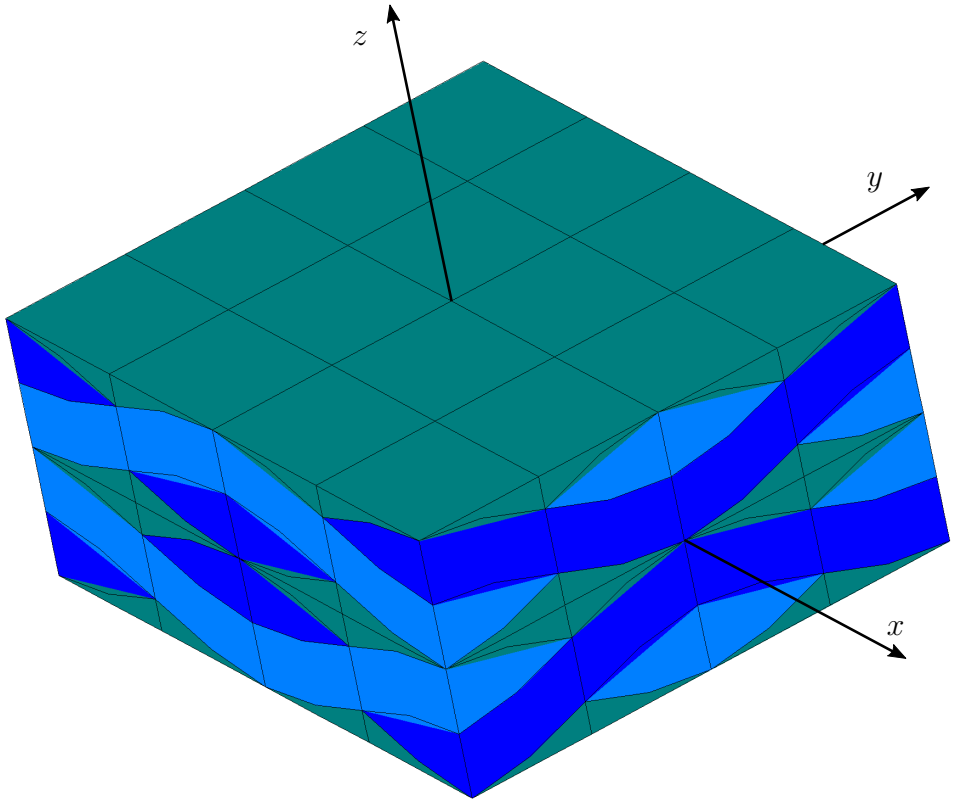

Figure 4.2: Full unit cell for symmetrically stacked plain weave

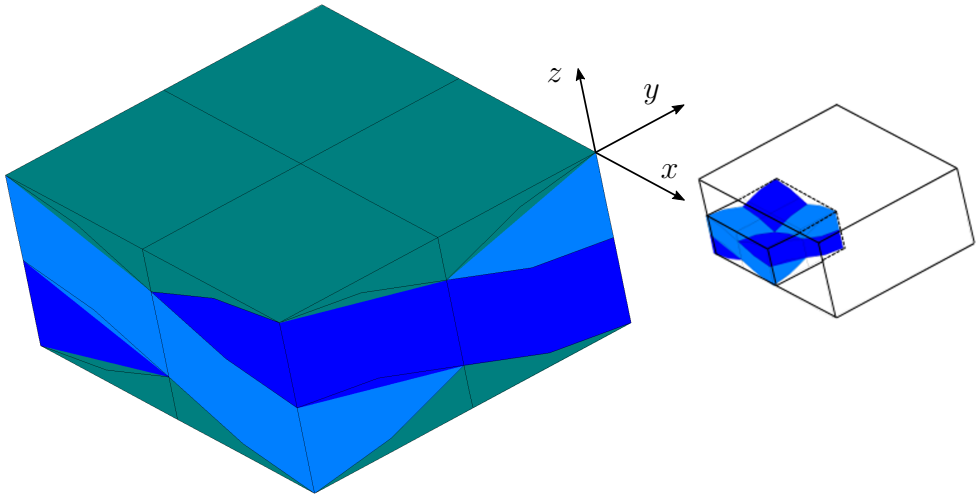

Figure 4.3: Eighth unit cell for symmetrically stacked plain weave

only 8 node hexahedron elements. The IMM meshes were constructed from the compatible mesh by removing the matrix elements, separating the tow elements into standalone entity meshes, and then supplying a structured background mesh which covered the volume originally occupied by the conventional matrix elements. This produces an IMM model with the exact same tow meshes, and a background mesh for the matrix with in-plane and through-thickness refinement identical to that of the conventional matrix mesh.

4.1.3 Boundary conditions

The plain weave unit cell was loaded uniaxially to 1% strain in the x direction, using periodic boundary conditions. The derivation of these boundary conditions is not discussed in this thesis. For a $1/8^{th}$ symmetrically stacked model, with the origin placed as shown in Figure 4.3, the periodic boundary conditions result in the following, for the faces with positive normal vectors:

$$u(0, y, z) = 0 \tag{4.2}$$

$$v(x, 0, z) = 0 \tag{4.3}$$

$$w(x, y, 0) = 0 \tag{4.4}$$

And for the faces with negative normal vectors:

$$u(-L, y, z) = -L \langle \varepsilon_{xx} \rangle = u_o \tag{4.5}$$

$$v(x, -W, z) = -W \langle \varepsilon_{yy} \rangle = v_o \tag{4.6}$$

$$w(x, y, -T) = -H \langle \varepsilon_{zz} \rangle = w_o \tag{4.7}$$

Where the parameters L, W, and H are the dimensions of the $1/8^{th}$ model in the

x, y, and z directions, respectively. Also the $\langle \varepsilon_{ij} \rangle$ are the volume average strains in the specified direction. Due to the material symmetry, and the condition of periodicity, the boundary conditions are such that the boundary faces must remain planar after deformation. The uniform displacements of these faces are denoted by u_o, v_o, and w_o for the x, y, and z faces respectively. The finite element code which was used to perform the conventional analyses herein already fully supports this type of loading. However, the code containing the IMM implementation does not have full support for the application of these boundary conditions. Because of this, and in order to apply the exact same loading to both models for purposes of comparison, the values of u_o, v_o, and w_o that result from the conventional analysis are used to apply uniform displacement boundary conditions to the faces of the IMM model.

4.2 Two-Inclusion

The two-inclusion model was designed to illustrate the effects of both the penalty displacement method, and its performance between two incompatibly meshed surfaces, one of which was created by the approximated background mesh. These effects are present in the plain weave model, but are obscured by the complex geometry and the dominance of the tows in carrying the applied load.

4.2.1 Geometry

The two-inclusion model consists of the cross sections of two circular inclusions in close proximity embedded in matrix. The close proximity of the inclusions is intended to amplify the stress gradients in the region between them. Sufficient matrix surrounds the inclusions to allow for the stress gradients to diminish before reaching the boundary of the model. Figure 4.4 shows the layout for the two-inclusion configuration.

In Figure 4.4, d is a spacing parameter determining the distance between the

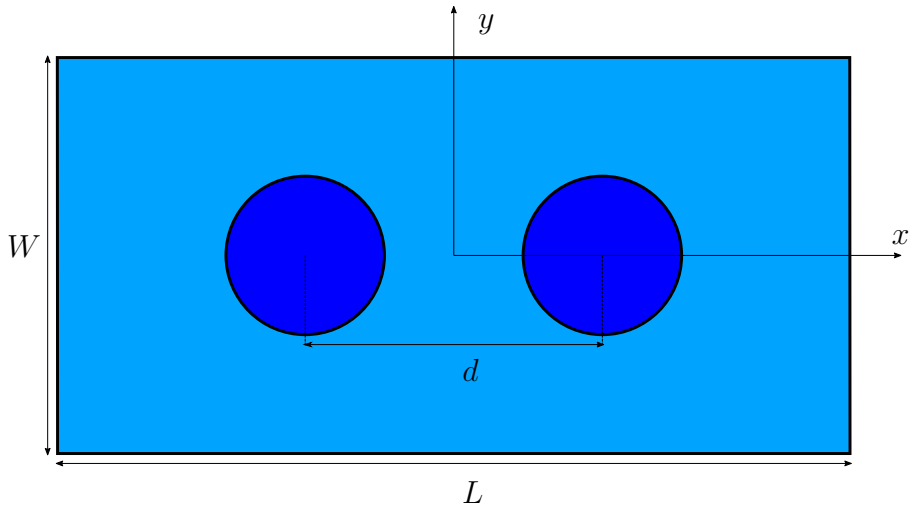

Figure 4.4: Tow-matrix model configuration

centers of the inclusions, which fall on the x axis equally spaced from the origin. The dimensions of the model are L, W, and H (not shown) in the x, y, and z directions. The model is three dimensional as required for the IMM. In addition, the finite element meshes for this configuration have more than a single element through the thickness to allow for automated penalty connections, which is a feature of the VTMS software. All of the dimensional parameters are derived from the inclusion radii, R, by the relations Equations 4.8-4.11.

$$L = 8R \tag{4.8}$$

$$W = 4R \tag{4.9}$$

$$H = 0.4R \tag{4.10}$$

$$d = 3R \tag{4.11}$$

4.2.2 Mesh

Like in the case of the plain weave model, the IMM mesh was constructed for the two-inclusion configuration by first obtaining a compatible mesh for the entire domain, then removing the matrix elements, separating the inclusion meshes into standalone entity meshes, and then supplying a structured background mesh for the matrix. In this configuration, only 8 node hexahedron elements were used for both the conventional and IMM meshes. The meshes used for this configuration are shown in Section 5.2.1.1 and Section 5.2.2.1 for the conventional and IMM analyses respectively.

4.2.3 Boundary conditions

The tow-matrix model was loaded under uniaxial strain in the x direction, while constraining the displacement of the y and z faces. The boundary conditions for all six faces are provided below.

$$u(\pm\frac{L}{2}, y, z) = \pm 0.075 \tag{4.12}$$

$$v(x, \pm\frac{W}{2}, z) = 0 \tag{4.13}$$

$$w(x, y, \pm\frac{H}{2}) = 0 \tag{4.14}$$

4.3 Material Properties

Both configurations make use of a common set of material properties. Each configuration contains two material groups, one is assigned the material properties of fiber-matrix tows, which exhibit transverse isotropy, and one is assigned the material properties of pure matrix, which is isotropic. The material properties for each are provided in Table 4.1. In the case of the two-inclusion model, the inclusions are

Table 4.1: Material properties for tows and matrix

Tow property	Value
$E1$	157.95 GPa
$E2, E3$	9.027 GPa
ν_{23}	0.3749
ν_{12}, ν_{13}	0.2412
G_{23}	3.34 GPa
G_{12}, G_{13}	5.12 GPa
Matrix property	**Value**
$E1, E2, E3$	3.1 GPa
$\nu_{23}, \nu_{12}, \nu_{13}$	0.35
G_{23}, G_{12}, G_{13}	1.15 GPa

assigned the material properties of the tows from Table 4.1.

In addition, the constitutive matrices that result from the properties listed in Table 4.1 are transformed from locally defined material coordinate systems into the global coordinate system at each node in the finite element mesh. In the plain weave model, for regions occupied by the tows, the local material orientations follow both the axial direction of the tow path as well as the local out of plane undulation in the tow. For the regions occupied by the matrix, the material orientation is irrelevant as the matrix is isotropic, and therefore the local material coordinate systems are aligned with the global axes. In the two-inclusion model, all material axes are aligned such that their first axis is aligned with the global z axis from Figure 4.4, with their second axis aligned with the global x direction.

5. RESULTS

This chapter presents the results for the evaluation of the IMM, beginning with the IMM's performance on the plain weave, followed by a description of the strategy used for identifying the cause of several issues with the IMM. Lastly the specifics of the lingering issues with the IMM are presented by investigating the two-inclusion model.

5.1 Plain Weave Model

The plain weave results are presented in three parts. First, results from a detailed conventional analysis are presented, and the metrics used to draw the comparisons to the IMM are introduced. The comparisons are made between the coarse meshes used in the two analysis methodologies, and the conventional results always serve as the benchmark, since if the IMM worked perfectly, then it would produce identical results. After the conventional results are presented, the initial results from the IMM are shown. It will be seen that these initial results contain irreconcilable differences which led to an in depth investigation, that ultimately produced an updated version of the IMM code. The investigation strategy used to discover the issues that were corrected is discussed in the next section. Lastly, the updated version of the IMM results is presented and the comparisons to the conventional results are made.

It is extremely important to note that since the tow meshes from the conventional analysis are used within the IMM analysis, this is a rather simplified use of the IMM. The IMM was created to manage completely incompatibly meshed tows, within a background mesh for the resin that is also completely incompatible with the tow meshes. Since the tow meshes from the conventional analysis are made from idealized geometry and contain perfect nodal compatibility, the IMM is not being challenged to

its full potential. It is known that the penalty connection is able impose displacement continuity between two mesh entities which have compatible surface meshes without causing error. Furthermore, since the tows are by far the predominant load carriers in the case of the textile analysis, the issues that the penalty connection causes in imposing displacement continuity between the tows and the matrix, which do not share compatibly meshed surfaces, are obscured.

5.1.1 Conventional plain weave analysis

The detailed conventional analysis begins with a convergence study to establish the necessary level of mesh refinement. The key metrics of the conventional analysis, that will also be produced from the IMM analysis and used for comparison, are then presented. These include the predicted effective axial modulus, locations of stress concentrations for the relevant stress components and their corresponding magnitudes, and a detailed look into the distributions of the stresses within the constituents.

5.1.1.1 Conventional mesh convergence study

The conventional mesh convergence study was performed using three meshes of the same configuration with increasing refinement. These meshes are shown in Figure 5.1. It can be seen that the middle (Figure 5.1b) and fine refinement meshes (Figure 5.1c) made use of a slightly different mesh architecture within the tows. This was because only the coarse mesh was restructured to be converted for use within the IMM analysis, where only linear 8 node hexahedron elements are supported.

The results of the convergence study are tabulated by their key metrics in Table 5.1. These metrics include the predicted effective axial modulus, the peak axial stress (in the material coordinate system), and the percent volume of material that is within 10% of the reported peak stress, denoted by $v_{10}^{Max}\ \sigma_{ij}$. The predicted axial

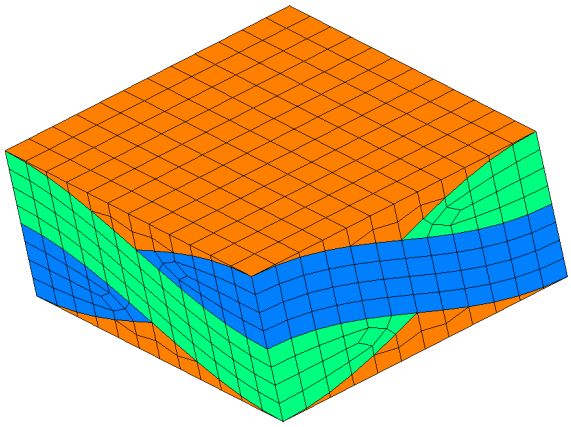

(a) Coarse mesh: 1728 elements

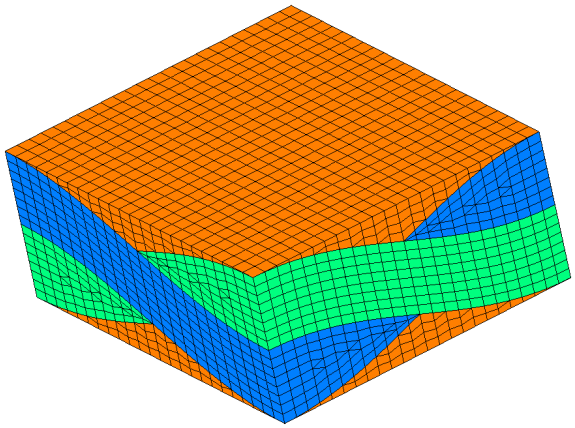

(b) Middle mesh: 13824 elements

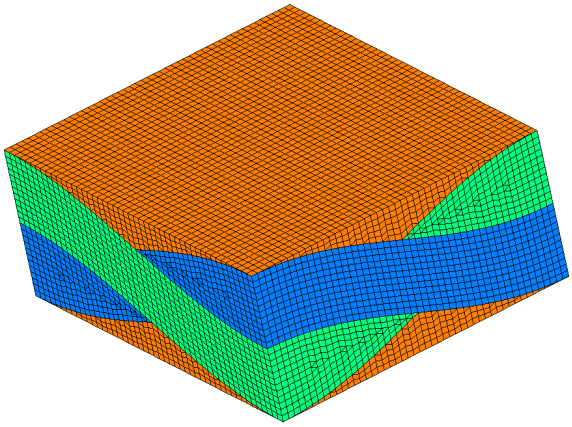

(c) Fine mesh: 66048 elements

Figure 5.1: Meshes used in convergence study of conventional analysis

Table 5.1: Key metrics from conventional mesh convergence study

Mesh	E11 (GPa)	Peak σ_{11} (Pa)	v_{10}^{Max} σ_{11}	Peak σ_{13} (Pa)	v_{10}^{Max} σ_{13}
Coarse	29.260	$1.3890E9$	1.02	$1.0239E8$	1.2
Middle	29.156	$1.4489E9$	0.20	$1.0447E8$	1.49
Fine	29.058	$1.5084E9$	0.01	$1.0426E8$	0.86

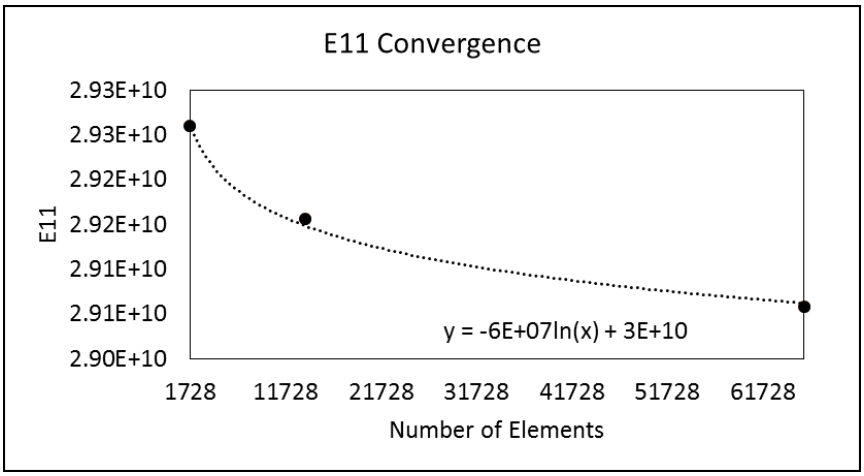

Figure 5.2: Mesh convergence of predicted effective modulus $E11$ for conventional analysis

modulus is shown to quickly converge, with a fine mesh value only 0.7% less than the coarse mesh value. Thus it is determined that the coarse mesh is sufficient for accurate results. The convergence of the predicted axial modulus is plotted in Figure 5.2. In addition it can be seen that the peak stress σ_{11} and its corresponding v_{10}^{Max} monotonically decrease. This is indicative that the stress concentration occurs at a small location.

The displacements of the unit cell's exterior faces are reported in Table 5.2 for the fine mesh. These displacements were used to evaluate the boundary conditions from Equation 4.7 which were applied to all of the IMM plain weave models.

Table 5.2: Facial displacements of fine mesh

u_o	-0.015
v_o	$1.9001972E-3$
w_o	$6.5488377E-3$

5.1.1.2 Locations of stress concentrations

The contour plots of the most relevant stress components, the stress in the direction of loading, σ_{11}, and the most significant resulting shear stress, σ_{13}, are displayed in the Figures 5.3 and 5.4. In these figures, the legends are scaled to the maximum and minimum stress for the elements that are shown. When the resin is displayed, the top half is hidden since it is simply mirrored about the xy plane. Due to the condition of periodicity, it can be seen that each of the displayed stress contours is symmetric through a 180 degree rotation about the z axis.

From Figure 5.3a it can be seen that the tensile σ_{11} stress concentration occurs in two locations. First, at the center of the mesh where the four tows intersect, within the axial tows. The axial tow is at its highest rotation angle at this point. Second, the tensile stress peaks within the axial tow where it shares a common interface with the transverse tow and is at is lowest rotation angle. The compressive stress concentration can be found along the sharp edge of the transverse tows. In Figure 5.3b the stress concentrations are found at the corners where the thickness of the resin material approaches zero. The tensile peak values are significantly higher than the compressive.

From Figure 5.4a several locations of peak σ_{13} stresses can be seen. The most significant positive stress concentration occurs in the interior of the axial tow at the location of highest rotation. A secondary concentration can be seen at center-width in the transverse tows at the location of half rotation (labeled with arrow in

Figure 5.4a). The most significant negative concentration occurs at center width in the axial tows near the location of zero rotation. A secondary concentration can be seen in the transverse tows spanning between the edges of the axial tows. In Figure 5.4b several concentrations of σ_{13} can be seen, but unlike the axial stress, the absolute values of the minimum and maximum are equal.

5.1.1.3 Stress volume distributions

The distributions of the σ_{11} and σ_{13} stress components within the volumes of the axial and transverse tows are plotted in Figures 5.5-5.8. These plots were created by determining how much volume is at or above a given stress level, ranging from the minimum to maximum stress. Like the contour plots, the stress ranges are adjusted to the maxima within the specified constituent. These figures quantify the information that is shown qualitatively through the contour plots. Some important characteristics of these curves can be interpreted. For example, a high slope (in magnitude, since all slopes here are negative) indicates that a significant portion of material is within a small range of stress. This behavior is also indicative of mild stress gradients. On the other hand a low slope is indicative of a severe stress gradient occurring over a small amount of material. The stress concentrations described previously can be identified among these curves with this interpretation. For example in Figure 5.8 the slope is rather constant which agrees with the gradients seen in the corresponding contour plot Figure 5.4a. This quantification of the visual representation is useful in drawing comparisons where the visual results are obscured.

5.1.2 Initial IMM plain weave analysis

5.1.2.1 Mesh

The mesh used to perform the initial IMM plain weave analysis is shown in Figure 5.9. The tow mesh, Figure 5.9a, is identical to the coarse conventional tow mesh

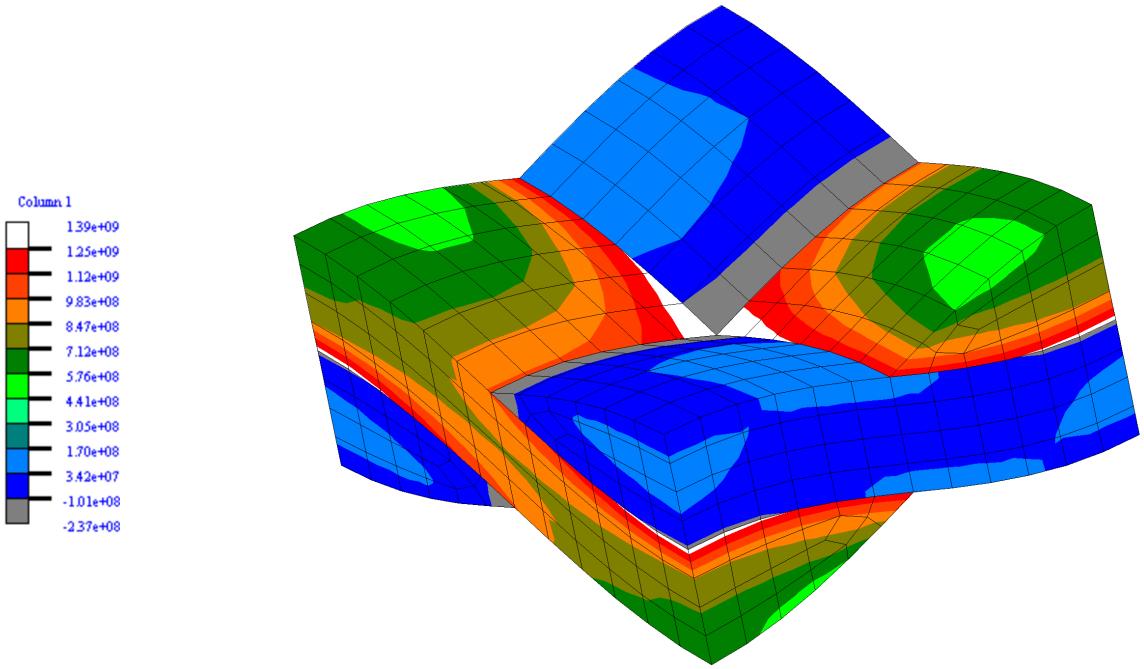

(a) Local σ_{11} distribution in tows

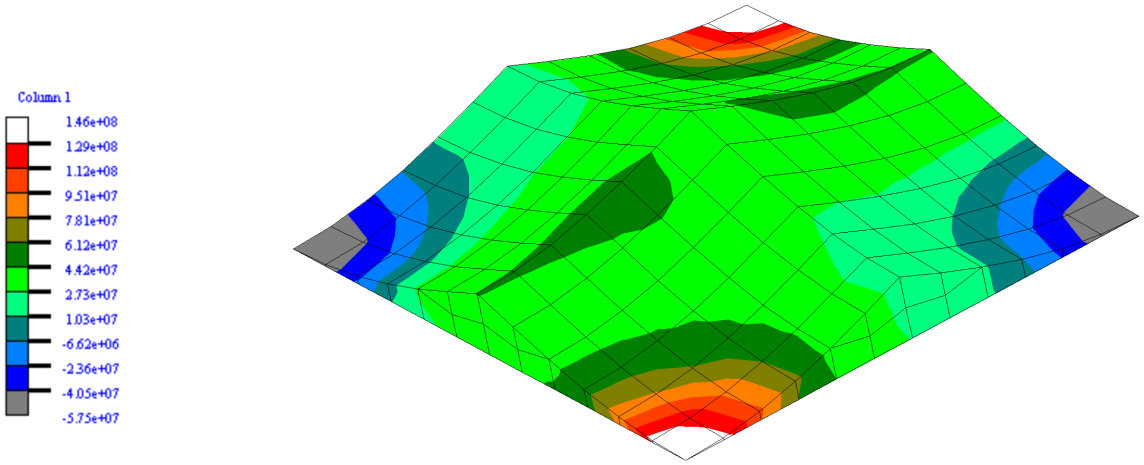

(b) σ_{11} distribution in resin

Figure 5.3: Contour plots of σ_{11} for coarse conventional mesh

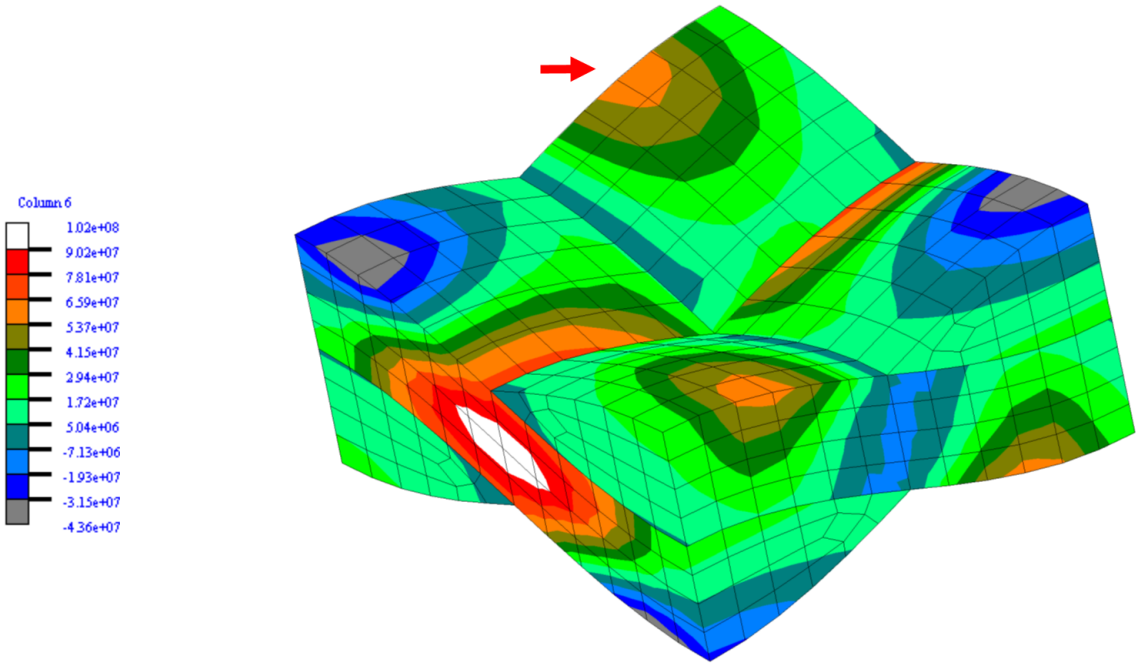

(a) Local σ_{13} distribution in tows

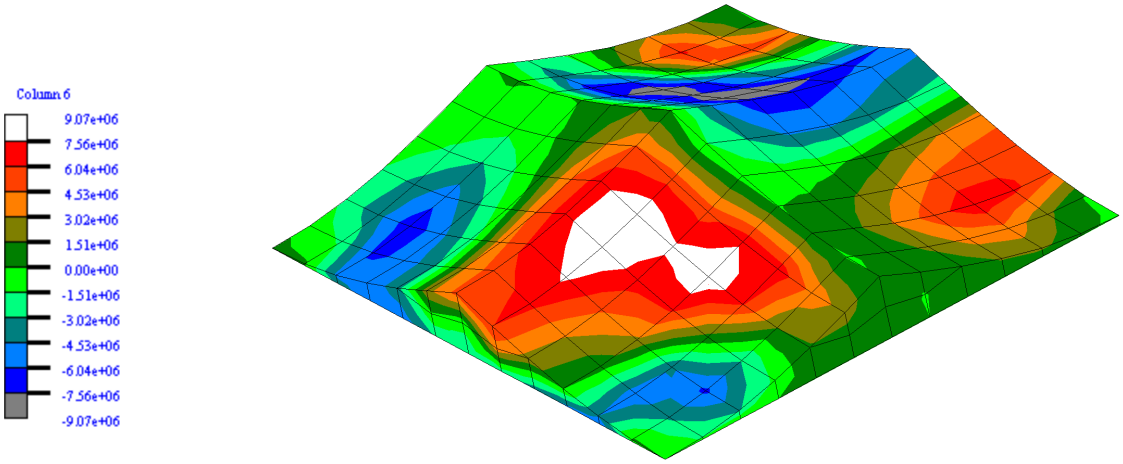

(b) σ_{13} distribution in resin

Figure 5.4: Contour plots of σ_{13} for coarse conventional mesh

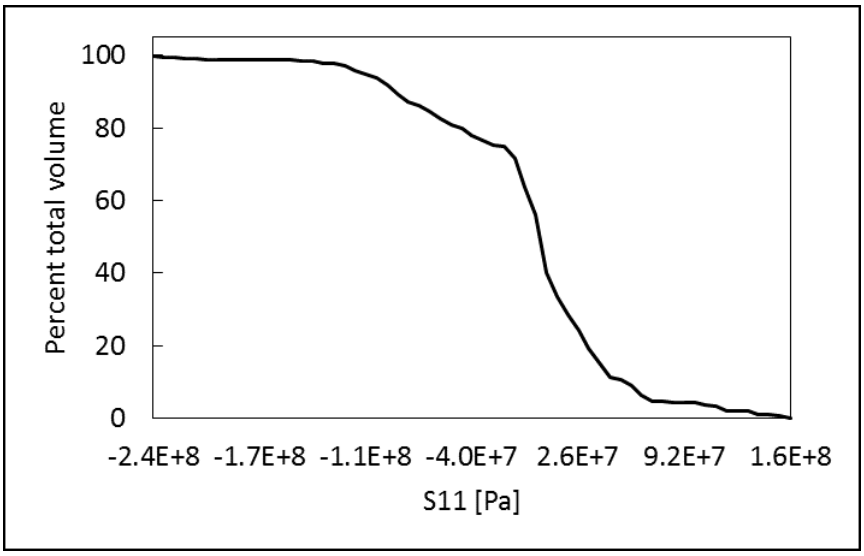

Figure 5.5: Conventional model distribution of σ_{11} within transverse tow

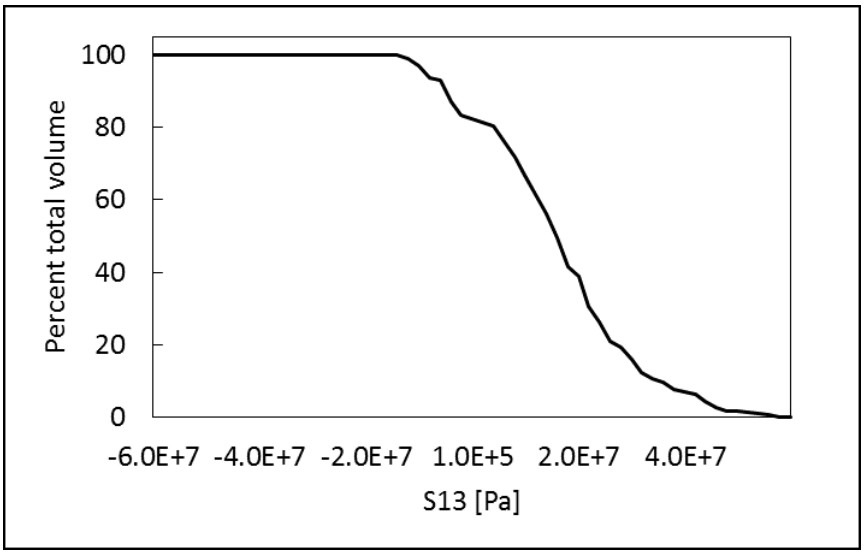

Figure 5.6: Conventional model distribution of σ_{13} within transverse tow

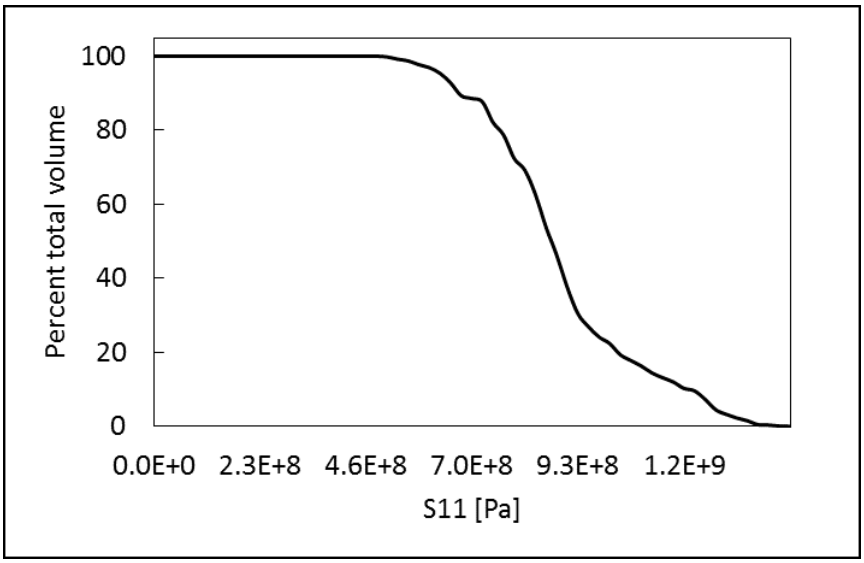

Figure 5.7: Conventional model distribution of σ_{11} within axial tow

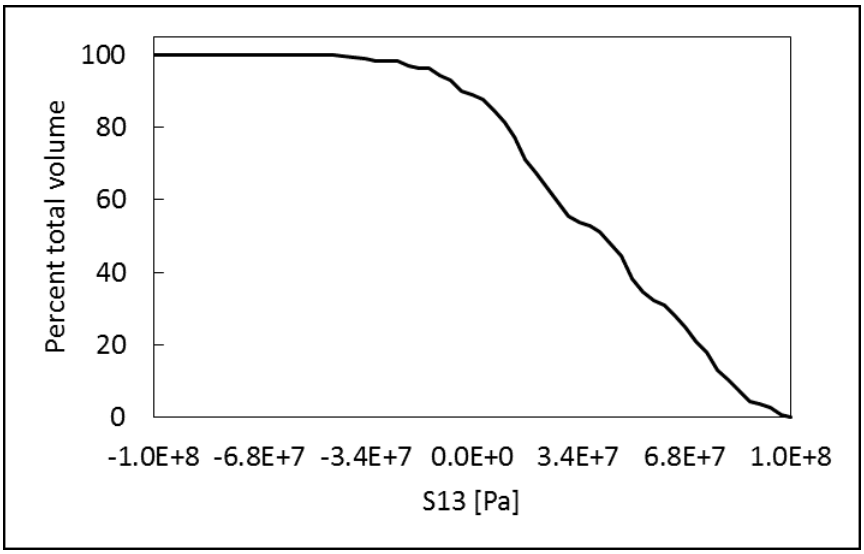

Figure 5.8: Conventional model distribution of σ_{13} within axial tow

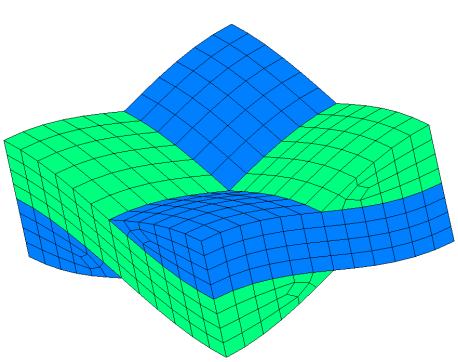

(a) Tow meshes: 960 elements total

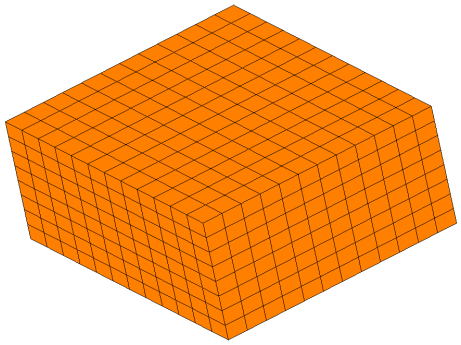

(b) Resin mesh: 697 elements (477 cut)

Figure 5.9: Meshes used for initial IMM analysis

in Figure 5.1a, save for separation of each tow into a standalone mesh. Although both of the axial tows and both of the transverse tows in Figure 5.9a are shown in the same color, the meshes are indeed standalone, meaning that there are spatially duplicate nodes all along the material interfaces, and that the penalty displacement method must be used to impose continuity across the material interface. The background mesh for the resin is shown in Figure 5.9b. It is a regular structured grid mesh with in-plane and through-thickness refinement equal to the tow meshes.

5.1.2.2 Key metrics

The key metrics from the initial IMM plain weave analyses are tabulated along with their error relative to those of the coarse conventional mesh in Table 5.3. As stated beforehand, these results contain significant error, which can be seen most prominently in the peak stresses, which are off by 26% in σ_{11} and by 40% in σ_{13}, as well as in the contour and volume distribution plots shown in the following sections.

Table 5.3: Key metrics for initial IMM analysis

Data	E11	Peak σ_{11}	v_{10}^{Max} σ_{11}	Peak σ_{13}	v_{10}^{Max} σ_{13}
Value	$30.30\,(GPa)$	$1.756E9\,(Pa)$	0.21	$0.6430E8\,(Pa)$	1.46
Error (%)	3.56	26.62	79.41	39.96	21.67

5.1.2.3 Locations of stress concentrations

The locations of the stress concentrations predicted by the initial IMM plain weave analysis are shown through contour plots, alongside those from the conventional analysis, in Figures 5.10 and 5.11. Each pair of plots is scaled to the same range. VTMS is used to plot the IMM results for the background mesh, as it has functionality for interpolating the stress data in the X3D8 elements. In these cases, the plot is still scaled to the same range as the conventional results, but the contours make use of a rainbow color spectrum with a larger number of bands. It is evident in Figure 5.10b that the initial IMM predicted different material behavior. There are several low stress concentrations in both the axial and transverse tows that are not present in the conventional results (labeled A and B in Figure 5.10b). In addition, the contour plot Figure 5.11b completely lacks the secondary positive stress concentrations in the transverse tows observed in the conventional results. The contours of the resin display similar behavior; however at different magnitudes. Also, the locations of σ_{13} peak stresses in the IMM resin (labeled with arrow in Figure 5.11d) are shifted towards the middle of the mesh.

5.1.2.4 Stress volume distributions

The initial IMM stress volume distributions for σ_{11} and σ_{13} within the axial and transverse tows are plotted along with the conventional results in Figures 5.12-5.15. The most prominent difference is observed in the plot of the σ_{11} distribution within

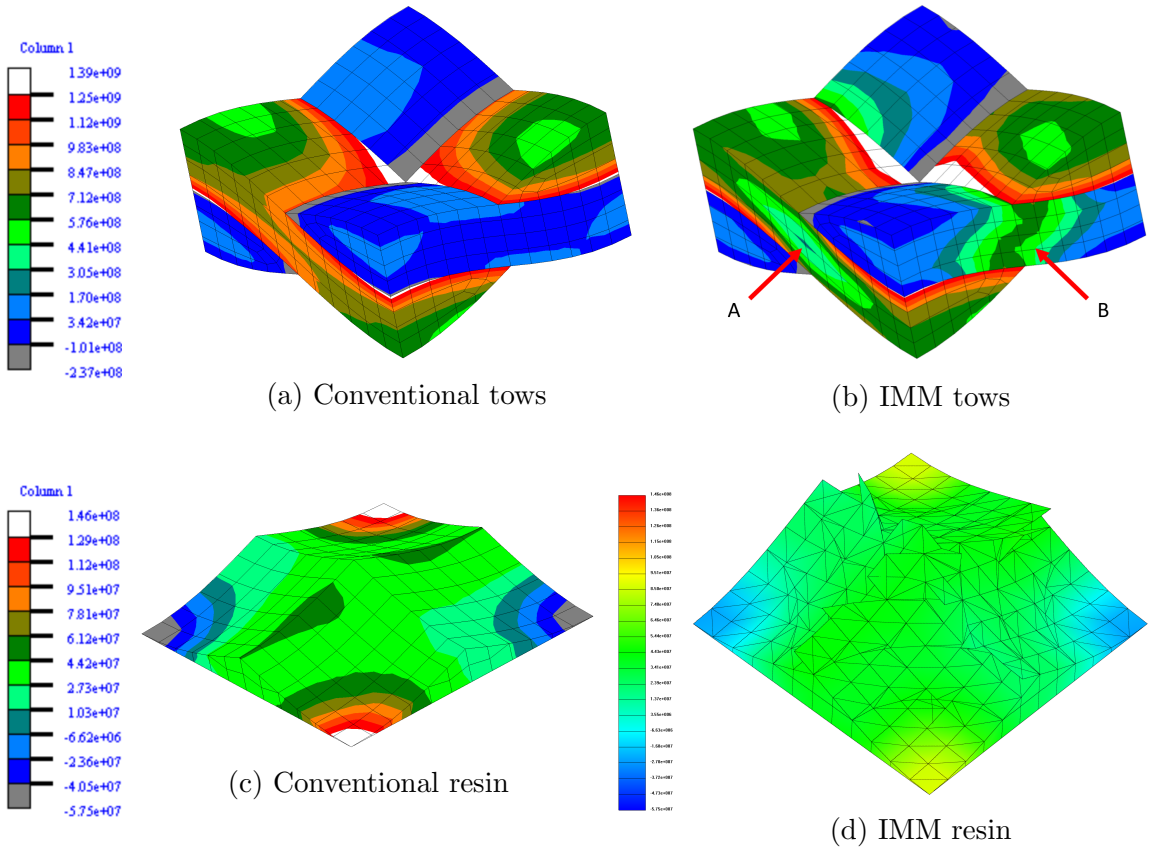

(a) Conventional tows

(b) IMM tows

(c) Conventional resin

(d) IMM resin

Figure 5.10: IMM initial: comparison plots of σ_{11} for coarse mesh

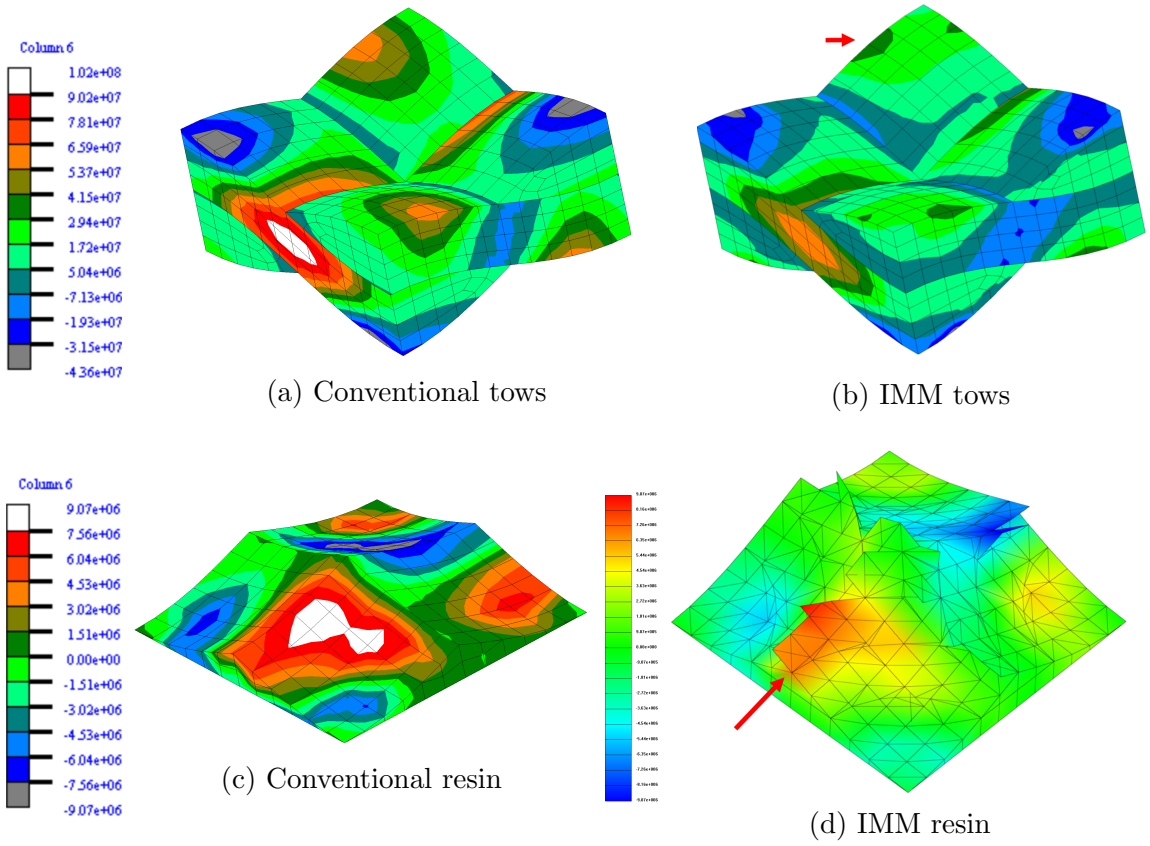

(a) Conventional tows

(b) IMM tows

(c) Conventional resin

(d) IMM resin

Figure 5.11: IMM initial: Comparison plots of σ_{13} for coarse mesh

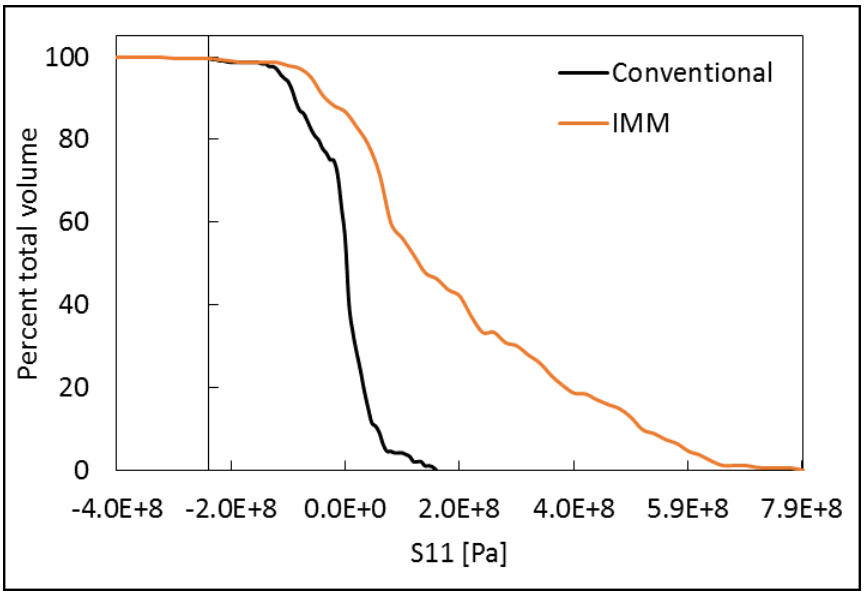

Figure 5.12: Initial IMM distribution of σ_{11} within transverse tow

the transverse tow in Figure 5.12. The IMM results curve shows different behavior. The plots of the σ_{13} volume distribution in the transverse tows, Figure 5.13, show similar behavior but shifted towards lower stress values. Likewise, the σ_{13} volume distribution in the axial tow, Figure 5.15, trends similarly to the conventional curve but towards a reduced peak stress. The separation between the curves in Figure 5.14 shows that the bulk of the initial IMM axial tow is at a lower stress than in the conventional results, and that there are higher gradients distributed through the bulk.

5.1.3 Correction strategy

With the observations made above from the Initial IMM plain weave analyses, an effort was made to investigate the cause for such significant disagreement between the two analyses. Since a substantial amount of time was spent correcting errors in the initial IMM, this section discusses the strategy used for systematically exploring

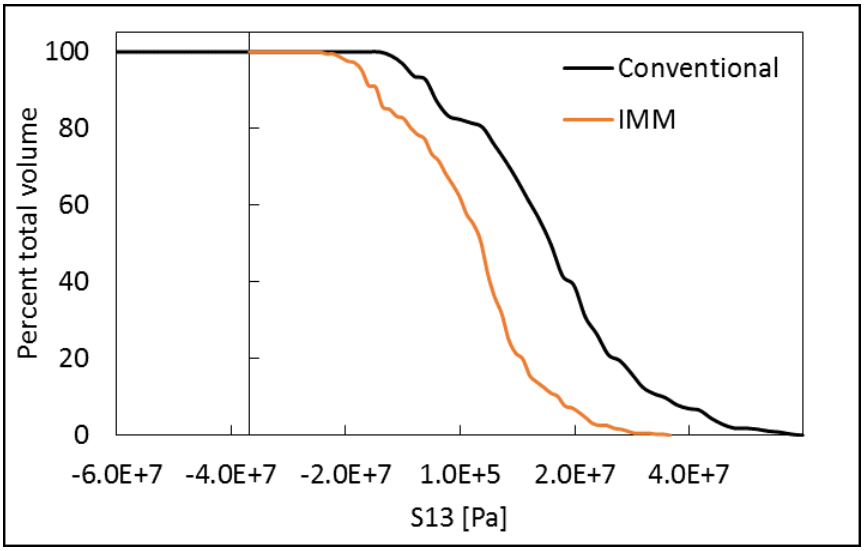

Figure 5.13: Initial IMM distribution of σ_{13} within transverse tow

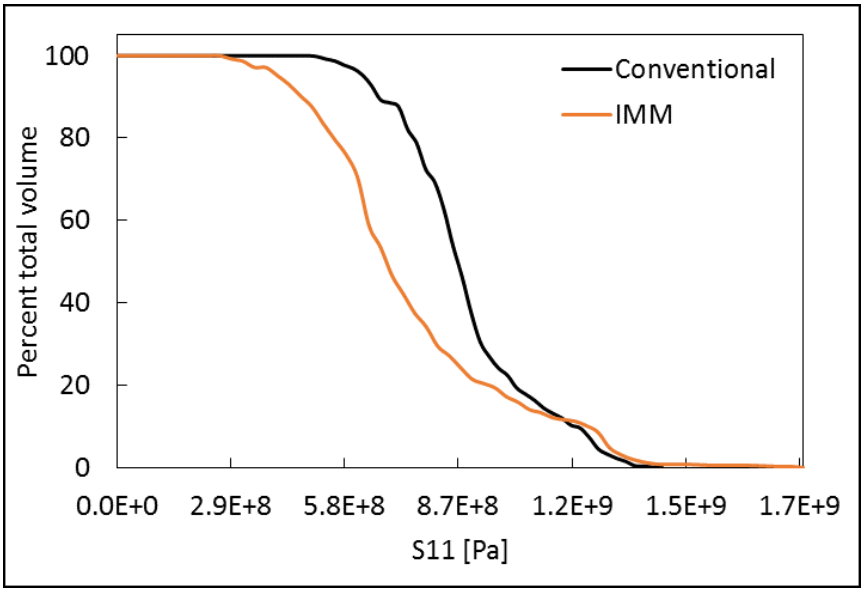

Figure 5.14: Initial IMM distribution of σ_{11} within axial tow

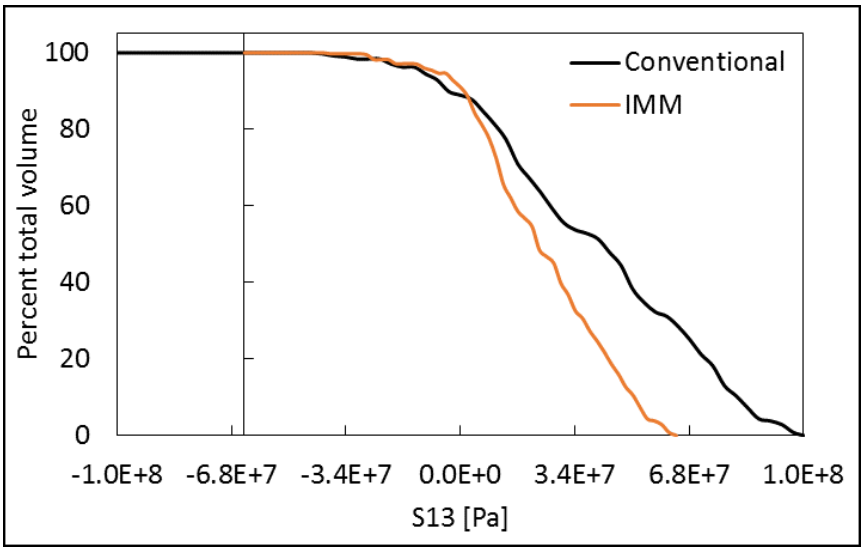

Figure 5.15: Initial IMM distribution of σ_{13} within axial tow

the IMM to discover the source of the errors. This strategy can be thought of as a top-down breakdown of the complexity involved in the plain weave analysis. By removing certain levels of analysis complexity, it was possible to determine what specific part of the code was responsible for the error. In a top-down fashion, the levels of complexity that were removed were:

- Inclusion of the background mesh. By removing the background mesh, the X3D8 elements were no longer in the picture.
- Separate entity meshes and use of the penalty displacement method. By recombining all of the tows into a single mesh, the penalty displacement method was removed from the picture. At this point, both of the identifying characteristics of the IMM were turned off, and the code should produce the exact same results as the conventional.
- Orthotropic material properties. By assigning a set of isotropic material properties to the entire mesh domain, the need for transformation of stiffness matrices

was removed.

- Material orientation. By aligning all of the local material coordinate systems with the global axes, the need to transform stresses was removed. At this point, the global and local results should be identical.

By following this paradigm it was discovered that once the material orientations were removed, the last item in the list, the results between the two analysis codes matched. This indicated a fundamental issue in stress transformations, which was corrected and resulted in an intermediately updated version of the IMM code. The investigation process was repeated using the updated code as significant issues were still present. This time, the analysis agreed when the second to last item in the list was removed, indicating an issue in transformation of stiffness matrices. This issue was corrected resulting in the final version of the IMM code. Needless to say, with the final version, the results between the two analyses agree completely when the first two items in the list, those that make up the IMM, are removed.

5.1.4 Final IMM plain weave analysis

After corrections were made to the IMM code by its authors, the results for the plain weave analysis were updated. In addition since significant improvements were made to the comparisons a convergence study was performed on the IMM analyses. The updated, or final IMM plain weave results, are presented in this section.

5.1.4.1 IMM mesh convergence study

The meshes used in the IMM mesh convergence study are shown in Figure 5.16. Again, the meshes for the tows in the coarse mesh are identical to those of the coarse conventional mesh. The refinements are then made on this coarse mesh. In each case, the background mesh for the resin is structured and has in-plane and

Table 5.4: Key values from IMM mesh convergence study

Mesh	E11 (GPa)	Peak $\sigma_{11}\,(Pa)$	$v_{10}^{Max}\ \sigma_{11}$	Peak $\sigma_{13}\,(Pa)$	$v_{10}^{Max}\ \sigma_{13}$
Coarse	30.257	$1.3262E9$	3.06	$1.0219E8$	1.46
Middle	27.072	$1.3879E9$	0.61	$1.0488E8$	1.55
Fine	27.313	$1.4701E9$	0.24	$1.0577E8$	1.34
Error	3.41 (%)	4.32 (%)	200.00 (%)	0.00 (%)	21.67 (%)

The error values are relative error between the coarse meshes of the conventional and IMM analyses for the respective data column

through-thickness refinements equivalent to those of the tows.

The key comparison metrics for each mesh in the convergence study are tabulated in Table 5.4. The errors between the coarse mesh metrics are appended to the end of the table. It can be seen that significant improvement has been made in the errors between the peak stresses, while the errors in the predicted effective modulus and v_{10}^{Max} metrics show less improvement.

The values of predicted effective modulus are plotted against mesh refinement in Figure 5.17. The converged value from the conventional mesh is plotted as the horizontal line. It is of note that the data points do not converge in a monotonic fashion (the points are fitted with a log curve). This behavior is suspected to be attributable to the number of X3D8 elements present in the refined models. As it will be seen later, the X3D8 elements are likely a major contributor to the remaining issues in the IMM, and as the number of them increases, the likelihood of significant errors being introduced increases. There are close to 8000 X3D8 elements in the fine mesh, while only 500 and 2000 in the coarse and middle mesh refinements, respectively. At any rate, the IMM seems to converge to $27.3GPa$, which is 6% less than the converged value of the conventional analysis.

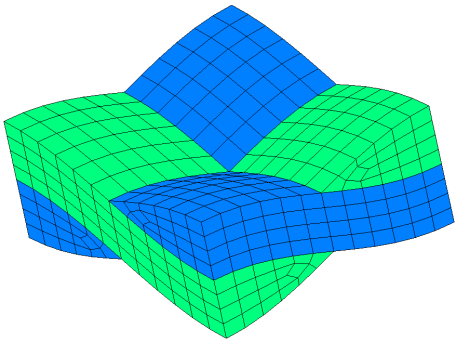

(a) Coarse mesh tows: 960 elements

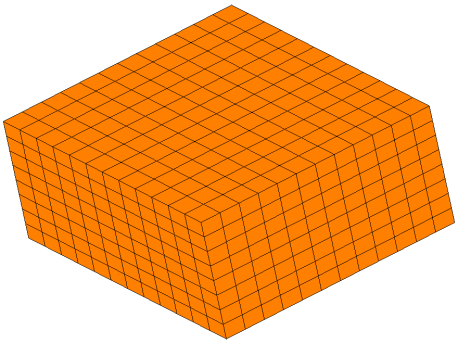

(b) Coarse resin: 697 elements (477 cut)

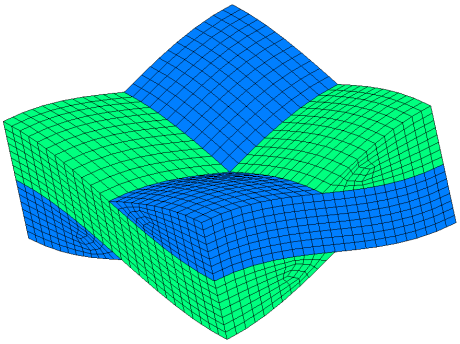

(c) Middle mesh tows: 7680 elements

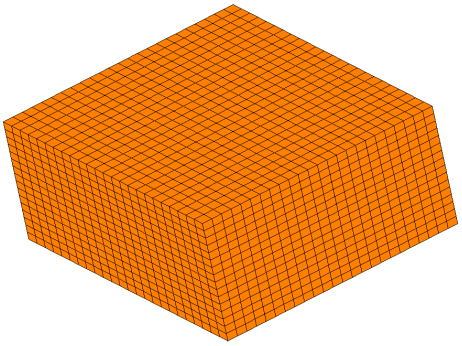

(d) Middle mesh resin: 4607 elements (1966 cut)

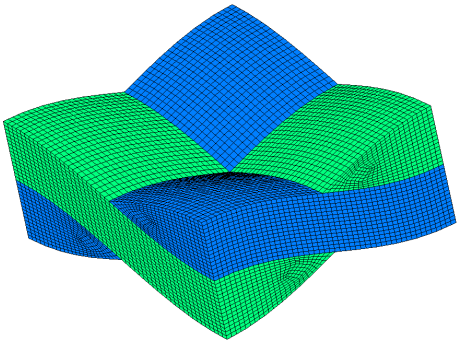

(e) Fine mesh tows: 61440 elements

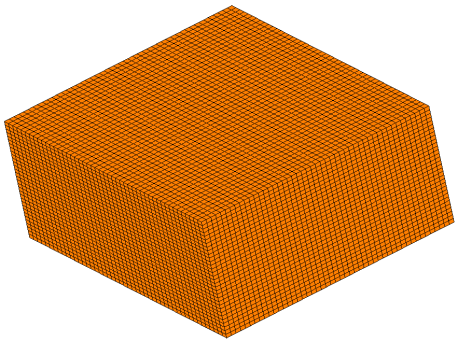

(f) Fine mesh resin: 32110 elements (7967 cut)

Figure 5.16: Meshes used in convergence study of IMM analysis

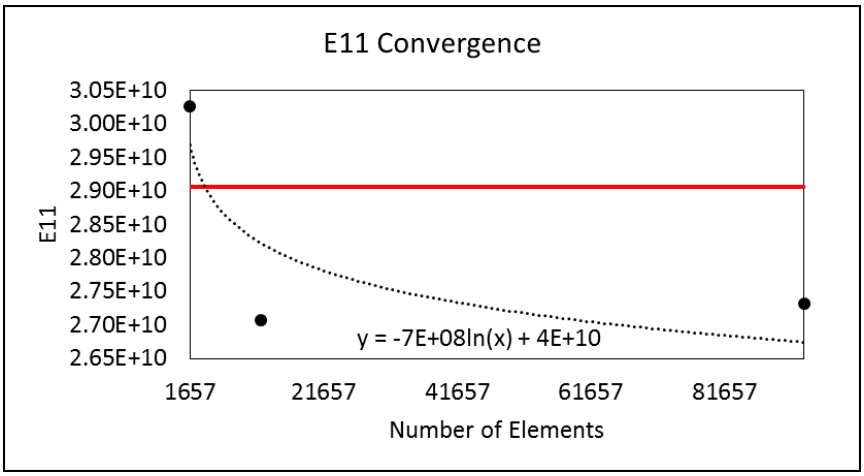

Figure 5.17: Mesh convergence of predicted effective modulus $E11$ for IMM analysis, showing the converged result from the conventional analysis as the horizontal

5.1.4.2 Locations of stress concentrations

The locations of the stress concentrations predicted by the final IMM analysis are shown through the updated contour plots of σ_{11} and σ_{13} in Figures 5.18 and 5.19. Huge improvement in the contours can be readily observed. All of the stress concentrations that were previously missing are now present, and those that were unexpectedly present are no longer. The most notable remaining differences are the slightly different shapes of the peak σ_{11} tensile stress concentration in the axial tows of Figure 5.18b, and the negative σ_{13} stress concentration in the axial tows labeled with an error in Figure 5.19b. These differences are reiterated in detail by the stress volume distribution plots.

5.1.4.3 Stress volume distributions

With the corrections to the IMM code, the stress volume distributions, like the contour plots, compare very well to the conventional results as can be seen by Figures 5.20a, 5.21a, 5.22a, and 5.23a. Because these curves compare so well, a zoomed

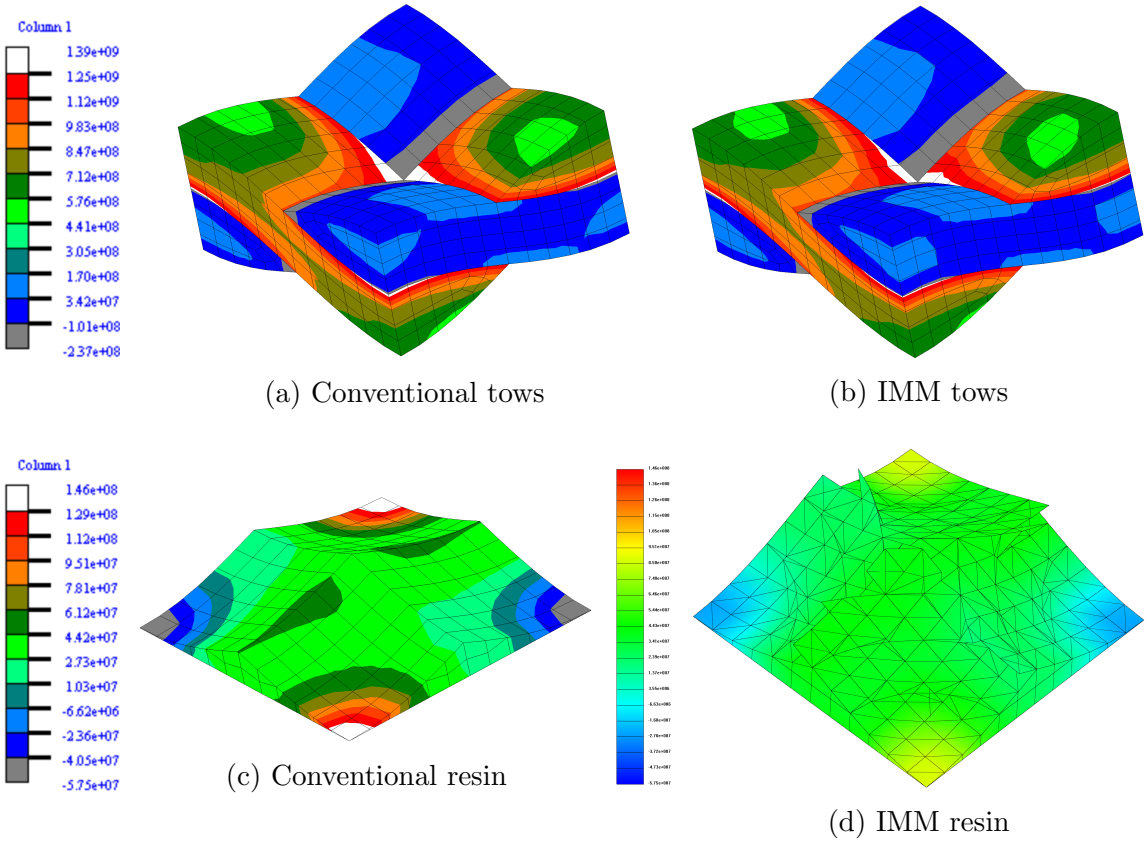

(a) Conventional tows

(b) IMM tows

(c) Conventional resin

(d) IMM resin

Figure 5.18: IMM final: Comparison plots of σ_{11} for coarse mesh

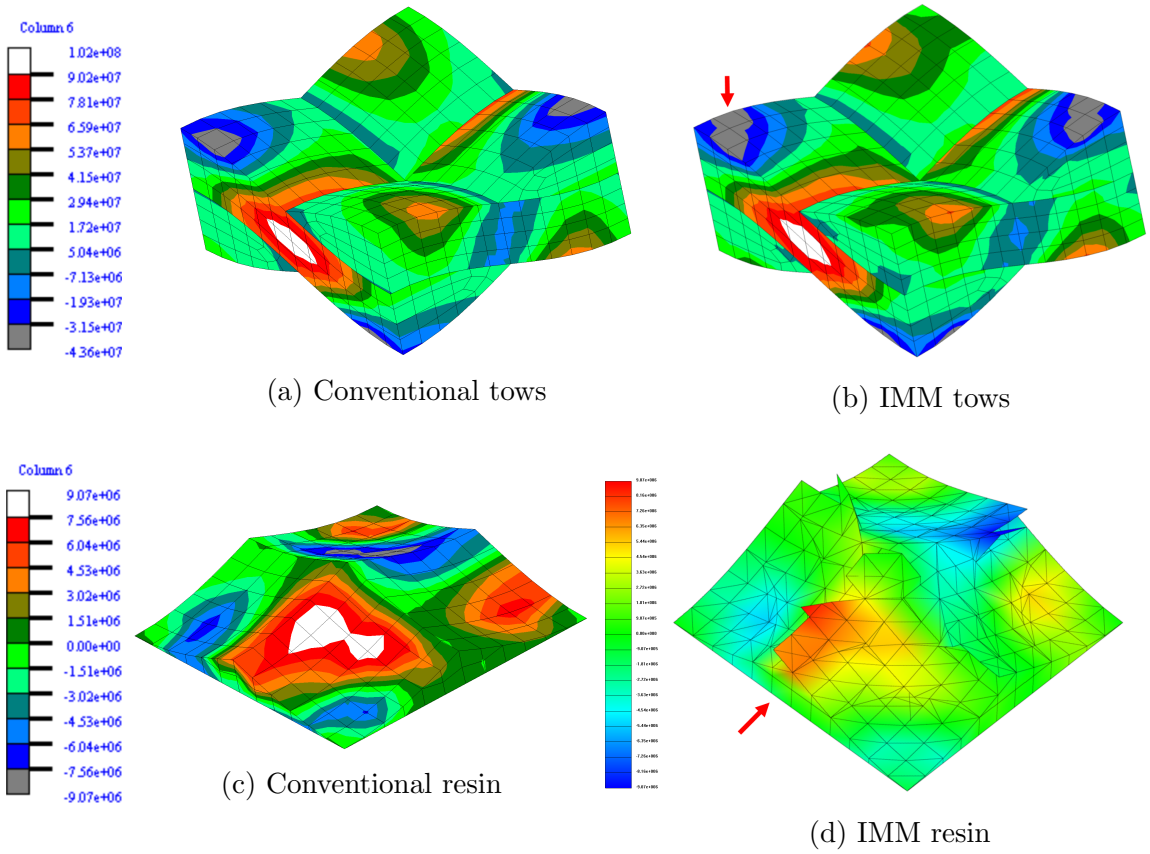

(a) Conventional tows

(b) IMM tows

(c) Conventional resin

(d) IMM resin

Figure 5.19: IMM final: Comparison plots of σ_{13} for coarse mesh

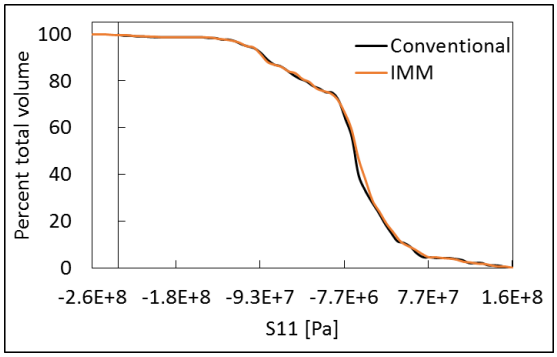

(a) Full range

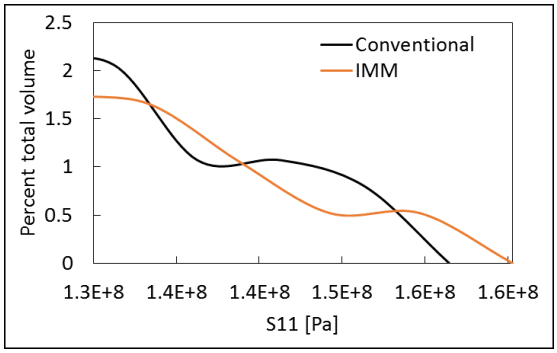

(b) Zoomed in view range

Figure 5.20: Final IMM distribution of σ_{11} within transverse tow

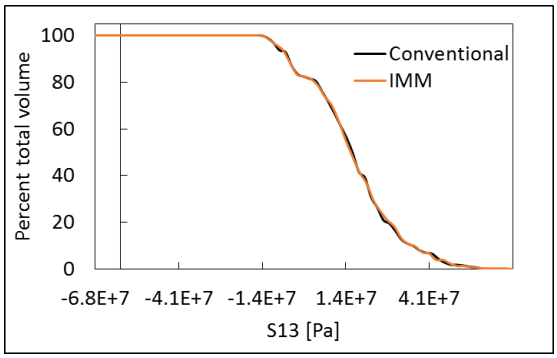

(a) Full range

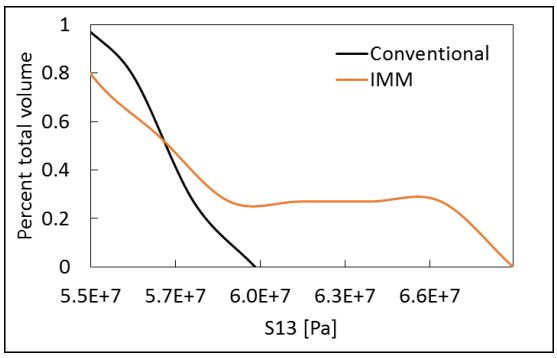

(b) Zoomed in view

Figure 5.21: Final IMM distribution of σ_{13} within transverse tow

in view of the top 20% stress values is supplied by adjusting the ranges of the figures. From these magnified plots, specifically Figure 5.21b, it can be seen that in some cases there are still some notable differences between the two analyses. These lingering differences are what led to the two-inclusion configuration and associated analyses.

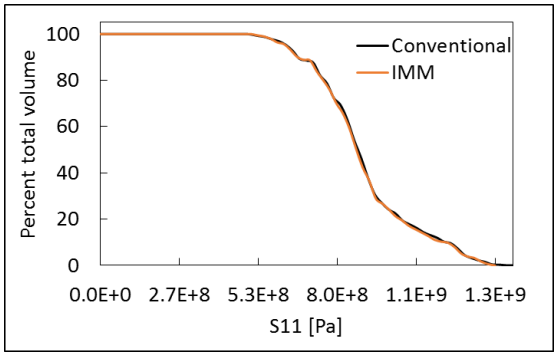

(a) Full range

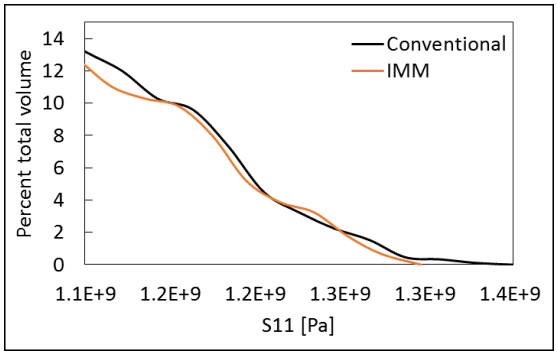

(b) Zoomed in view

Figure 5.22: Final IMM distribution of σ_{11} within axial tow

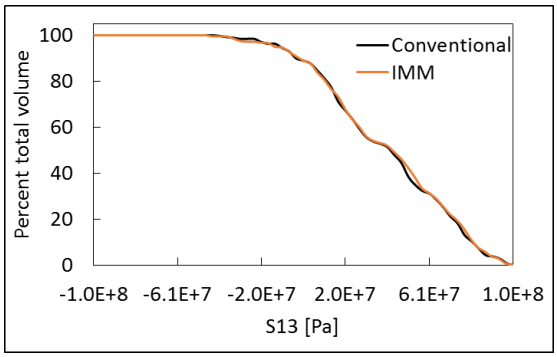

(a) Full range

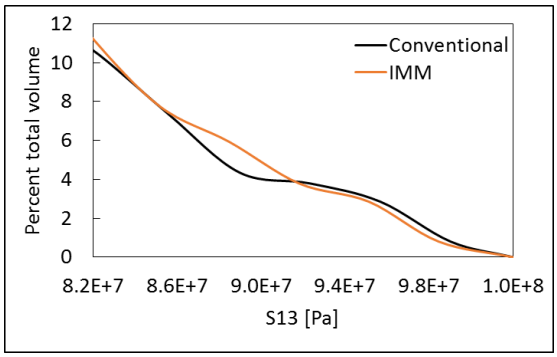

(b) Zoomed in view

Figure 5.23: Final IMM distribution of σ_{13} within axial tow

5.2 Two-Inclusion Model

The results for the two-inclusion model are presented similarly to those of the plain weave. First the conventional results are presented to serve as the benchmark. Then the IMM results are presented and discussed. However, since the two-inclusion model is designed to specifically investigate the performance of the penalty based material interfaces, the effects of the IMM penalty coefficient parameter are presented through a penalty convergence study. In order to provide further insight into the characteristics of these penalty connections, two simplified cases are presented after the regular IMM analysis. The first is a simplified model where the entire mesh is assigned the material properties of the resin from Table 4.1. With this modification, and the fact that the model is loaded uniformly, any perturbation from the state of iso-stress can be attributed to a failure in the penalty connection. Second, a simplified analysis that makes use of the penalty connection between incompatible meshes without X3D8 elements is presented.

5.2.1 Conventional analysis

Results from the conventional two-inclusion analysis are presented in this section.

5.2.1.1 Conventional mesh convergence study

A convergence study was performed for the conventional mesh using four meshes of increasing refinement. The meshes used are shown in Figure 5.24. The key metrics from each refinement are provided in Table 5.5, and the convergence of the predicted elastic modulus is plotted in Figure 5.25. In this analysis, the first axis all of the material coordinate systems are aligned in the direction of the global z axis (refer to Figure 4.4). Because of this the predicted effective axial modulus, $E11$, converges to a value that is similar to the transverse elastic moduli of the tow material properties

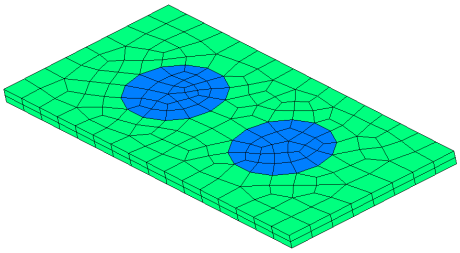

(a) Mesh 1: 402 elements

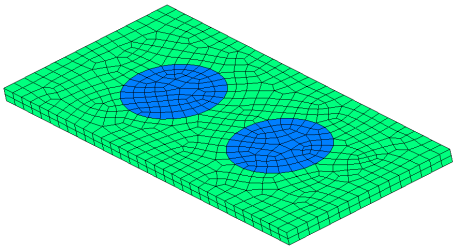

(b) Mesh 2: 1318 elements

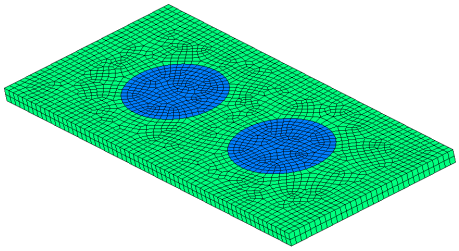

(c) Mesh 3: 4758 elements

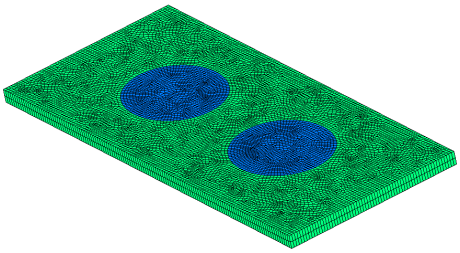

(d) Mesh 4: 20714 elements

Figure 5.24: Meshes used for conventional Two-Inclusion study

Table 5.5: Tabulated results from conventional Two-Inclusion analyses

Refinement	Effective Modulus $E11\,(GPa)$	Peak $\sigma_{11}\,(Pa)$	$v_{10}^{Max}\ \sigma_{11}$
Mesh 1	5.6444	$1.4086E8$	4.6
Mesh 2	5.6561	$1.3786E8$	5.62
Mesh 3	5.6596	$1.3613E8$	9.26
Mesh 4	5.6604	$1.3474E8$	13.99

from Table 4.1. The difference in the predicted values of the effective modulus between the finest mesh, Mesh 4, and the coarsest mesh, Mesh 1, shown in Table 5.5 is 0.3%.

5.2.1.2 Location of stress concentrations

The locations of stress concentrations for the conventional two-inclusion analysis are shown in Figure 5.26. From Figure 5.26a, it can be observed that the peak tensile stress concentration occurs within the matrix, at the points on the material interface

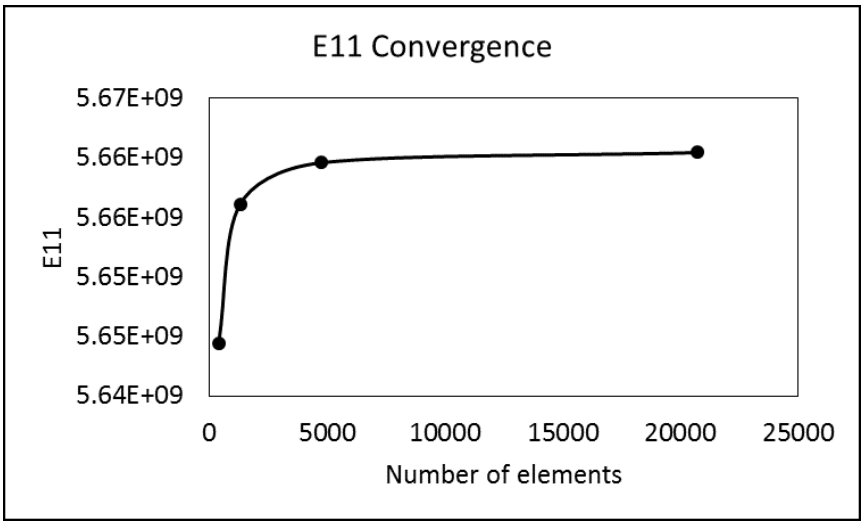

Figure 5.25: Convergence of predicted elastic modulus for conventional Two-Inclusion study

where the inclusions are closest together. The peak compressive stress concentrations occur in the matrix at the material interface on the flanks of the inclusions. Also the stresses in the inclusion are nearly all within the same color band, indicating a nearly uniform stress state. In Figure 5.26b the matrix has been hidden and the contour legend has been adjusted to the maximum and minimum stress within the elements shown. It can be seen that there is a consistent gradient ranging from maximum tensile at the point closest to the adjacent inclusion, to minimum on the opposite side of the inclusion.

5.2.2 IMM analysis

Results from the regular IMM two-inclusion analysis are presented in this section.

5.2.2.1 IMM convergence studies

Two convergence studies were performed for the IMM two-inclusion analyses. First, the convergence with respect to penalty parameter is presented for each mesh

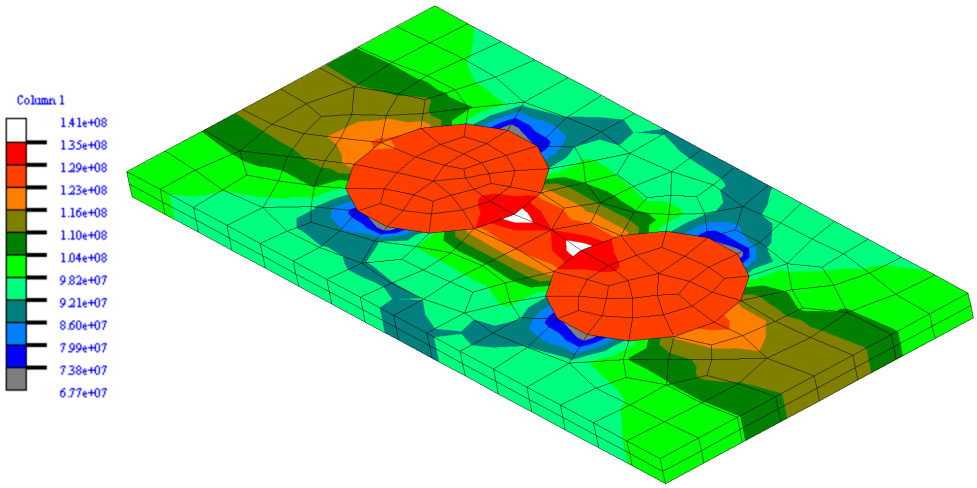

(a) Global σ_{11} distribution

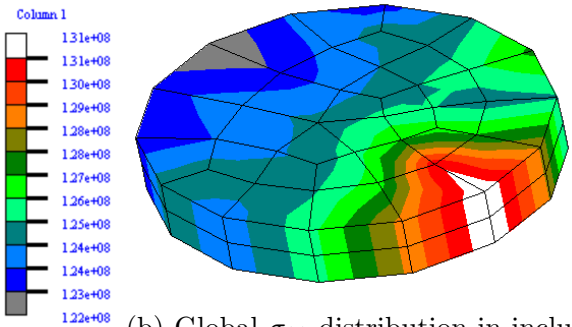

(b) Global σ_{11} distribution in inclusion

Figure 5.26: Contour plots of σ_{11} for coarse conventional mesh

refinement. Second, the convergence with respect to mesh refinement for each penalty parameter is presented. The penalty parameters were varied from slightly below the suggested value all the way up to values that cause numerical instability in the code. The penalty values used were $[1E10, 1E11, 1E12, 1.052E12, 1E13, 1E16, 1E19, 1E22]$, and the meshes used are shown in Figure 5.27.

The convergences of predicted effective modulus for each mesh refinement with respect to penalty parameter is plotted in Figure 5.28. It can be seen from the curves that the two less refined meshes do not exhibit the same behavior as the two more refined meshes. Because of this Mesh 1 and Mesh 2 are not quite converged, with respect to penalty, until a penalty of $1E16$, while the more refined meshes are converged by the suggested penalty of $1.052E12$.

The convergence of predicted effective modulus for each penalty parameter with respect to mesh refinement is plotted in Figure 5.29. It is evident from these curves, that the two lowest penalty values are not sufficient. Since the penalty parameter is analogous to a stiffness coefficient for the bond of the material interface, a value too low will not impose sufficient displacement compatibility at the material interface and allow stresses to relax, leading to a lower predicted stiffness. The four highest penalty values converge to a similar predicted effective modulus.

Key metrics from the convergence study, and their errors relative to the conventional results, are presented in Table 5.6. The values are from the coarse mesh, Mesh 1, for the suggested and the converged penalty parameters. While the errors associated with the predicted effective modulus are tolerable, those related to the peak stresses are significant.

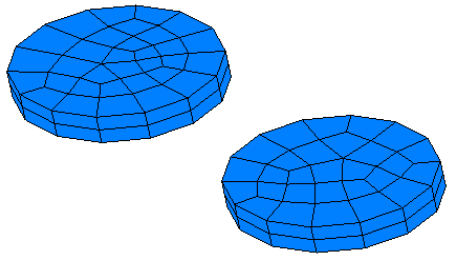

(a) Mesh 1 inclusions: 120 elements

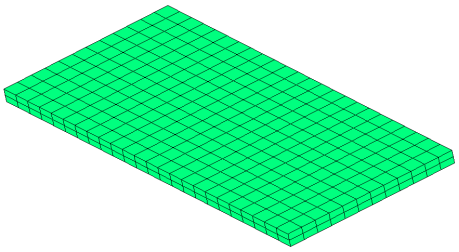

(b) Mesh 1 matrix: 512 elements (88 cut)

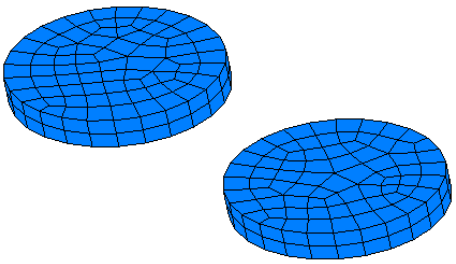

(c) Mesh 2 inclusions: 306 elements

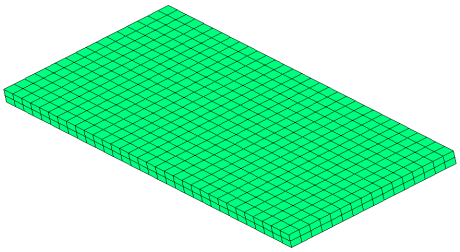

(d) Mesh 2 matrix: 896 elements (128 cut)

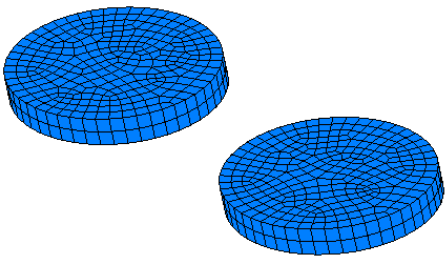

(e) Mesh 3 inclusions: 1122 elements

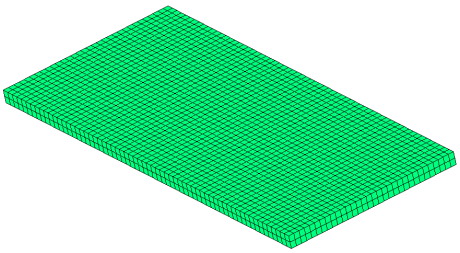

(f) Mesh 3 matrix: 3440 elements (256 cut)

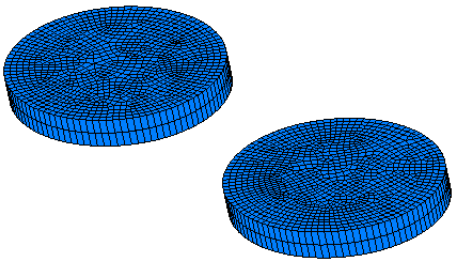

(g) Mesh 4 inclusions: 4672 elements

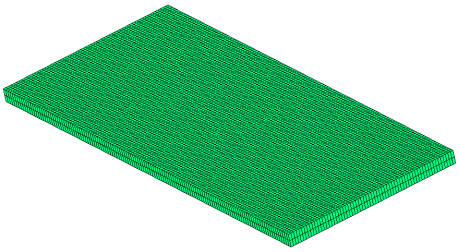

(h) Mesh 4 matrix: 13456 elements (512 cut)

Figure 5.27: Meshes used for IMM Two-Inclusion study

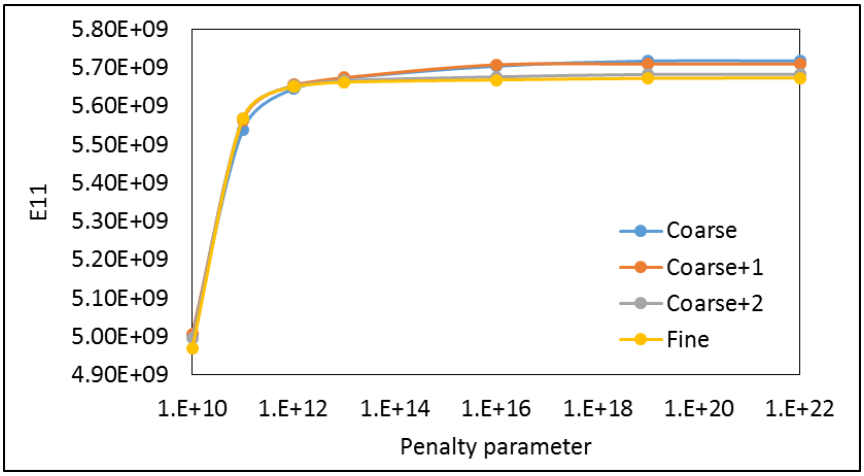

Figure 5.28: Convergence of predicted modulus with respect to penalty parameter for each mesh

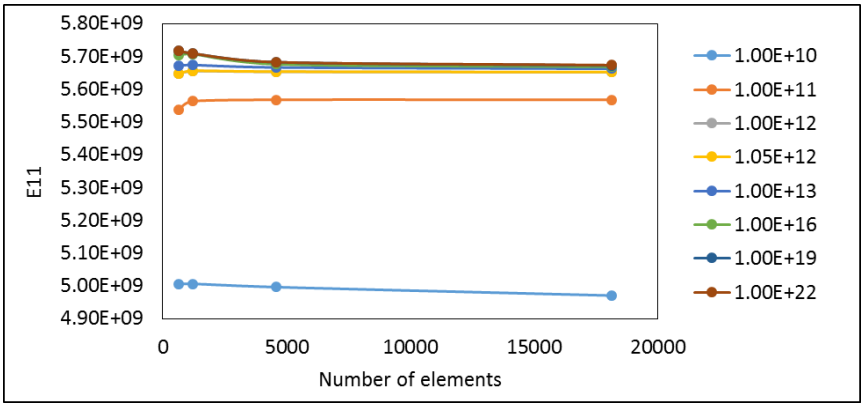

Figure 5.29: Convergence of predicted modulus with respect to mesh refinement for each penalty parameter

Table 5.6: Key metrics from IMM Two-Inclusion analyses

PP	Modulus (GPa)	Error	Peak $\sigma_{11}\,(Pa)$	Error	$v_{10}^{Max}\ \sigma_{11}$	Error
1.052E12	5.6475	0.05	1.6195E8	14.89	0.53	88.48
1E16	5.7035	1.05	1.7246E8	21.99	0.25	94.57

5.2.2.2 Locations of stress concentrations

The locations of stress concentrations within the IMM two-inclusion model are shown in Figure 5.30, for the suggested penalty parameter, and Figure 5.31, for the converged penalty value. The contours of the conventional analyses are shown alongside, and each plot is scaled to the same range as shown. While the contours of Figure 5.30a and 5.31a seem to exhibit similar characteristics, the contours on the inclusions alone do not. Figures 5.30d and 5.31d show a stress distribution that is highly distorted by a failure in the penalty interface connection. Since the boundary conditions are uniform, and the mesh is identical in the xy plane through the thickness, there is absolutely no reason for there to be any variation of stress through the thickness. Not only do the stresses from the IMM analyses vary through the thickness of the inclusions, they also have completely erratic distributions throughout the inclusion.

5.2.3 Simplified case: single material property

The single material property simplification for the two-inclusion model is presented to show the error that is directly related to the penalty connection between the master and background meshes. For these analyses, the coarse mesh is used. After applying a single set of material properties to the entire mesh, those of the tow in Table 4.1, the conventional analysis predicts an axial elastic modulus of $9.01GPa$. This value is indeed close to the assigned value of $E2$ (recall the material is aligned with the first axis out of plane, such that the local y axis is aligned in the global x direction); it differs slightly due to the restriction of the Poisson contractions in the boundary conditions.

A penalty-convergence study was performed for the single property IMM analyses to check for any modified convergence behavior. The convergence of the predicted

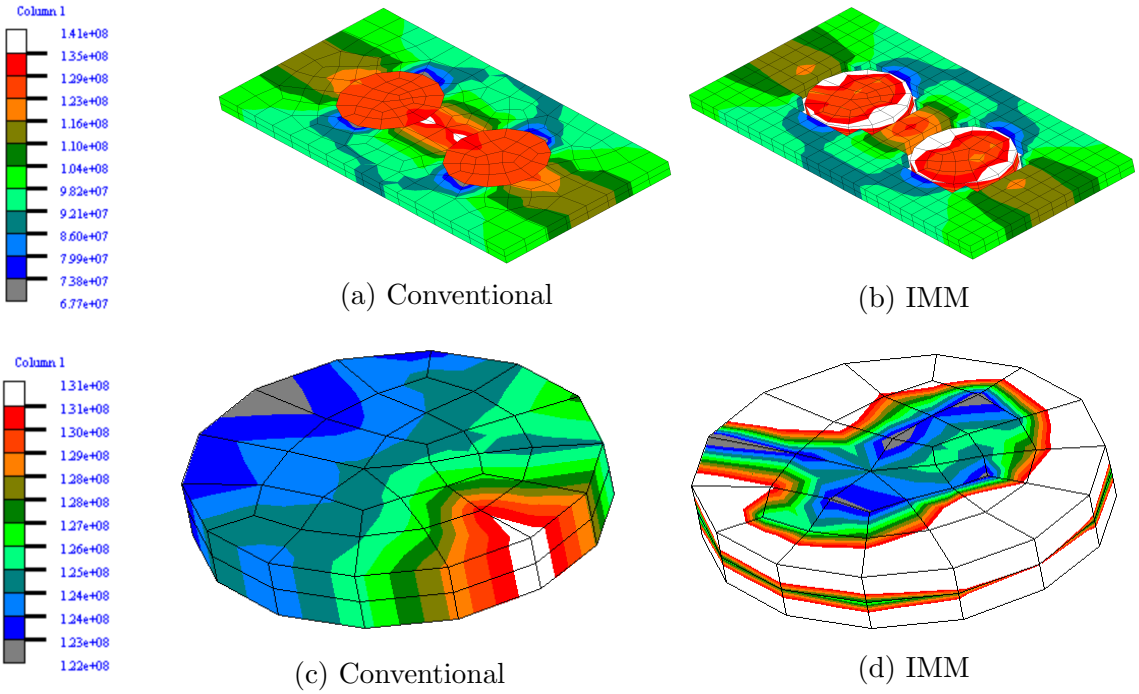

(a) Conventional (b) IMM

(c) Conventional (d) IMM

Figure 5.30: Contour plots of σ_{11} for IMM using suggested penalty

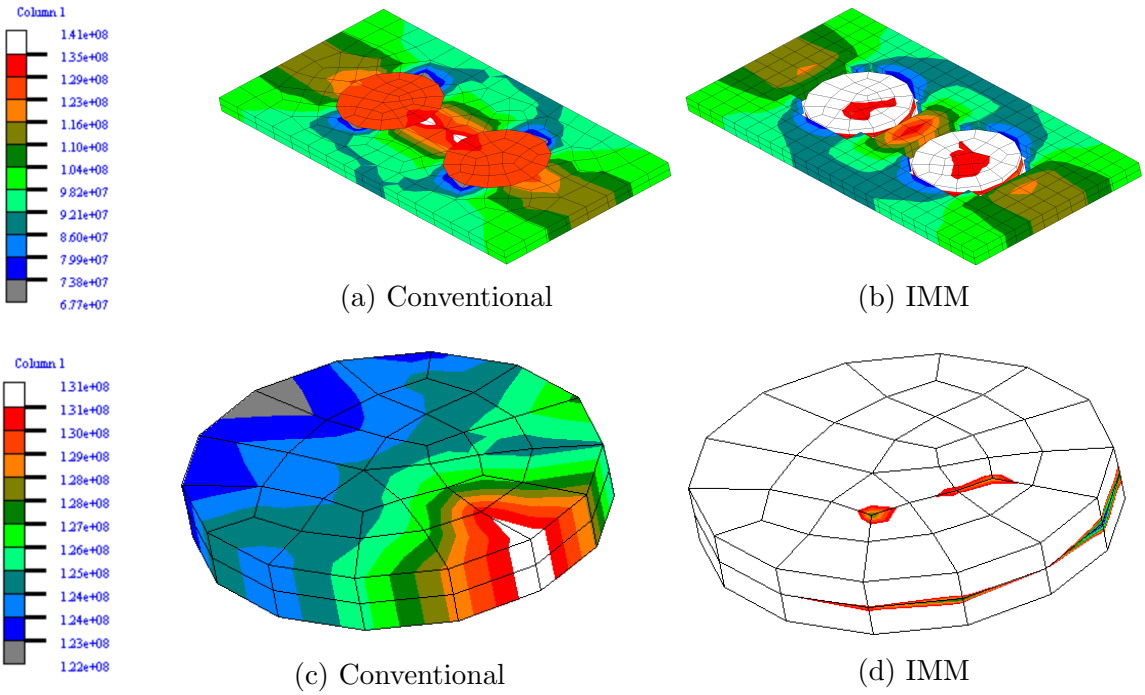

(a) Conventional (b) IMM

(c) Conventional (d) IMM

Figure 5.31: Contour plots of σ_{11} for IMM using converged penalty

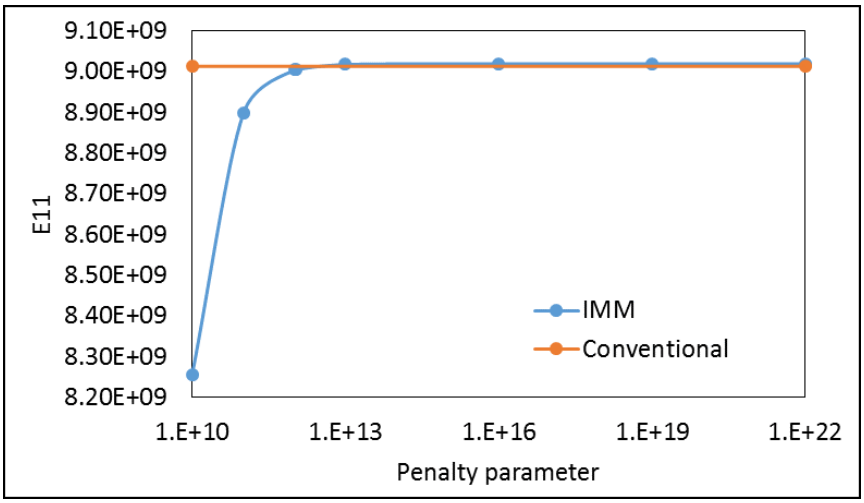

Figure 5.32: Convergence of single property IMM Two-Inclusion model with respect to penalty parameter

effective modulus is plotted in Figure 5.32. It can be seen that with the modified material properties, the coarse mesh converges monotonically with respect to penalty parameter like the two fine meshes did beforehand. This suggests that the irregularity in the two coarse mesh curves of Figure 5.28 is not solely related to the mesh.

Contour plots of the axial stress for the suggested and converged penalties are shown in Figure 5.33. In these contour plots, any stress gradient is an error caused directly by the penalty connection. Both plots of the IMM results contain similar errors in the matrix elements around the inclusion. The position of these errors, namely the four corner elements, suggest that the penalty connection does not well manage X3D8 elements which are heavily intersected by master surfaces.

5.2.4 Simplified case: rotated inclusion

The last results that are presented are for the simplified case where the conventional two-inclusion mesh was modified to be incompatible at the material interface. By doing this, the penalty connection can be implemented between two incompatibly

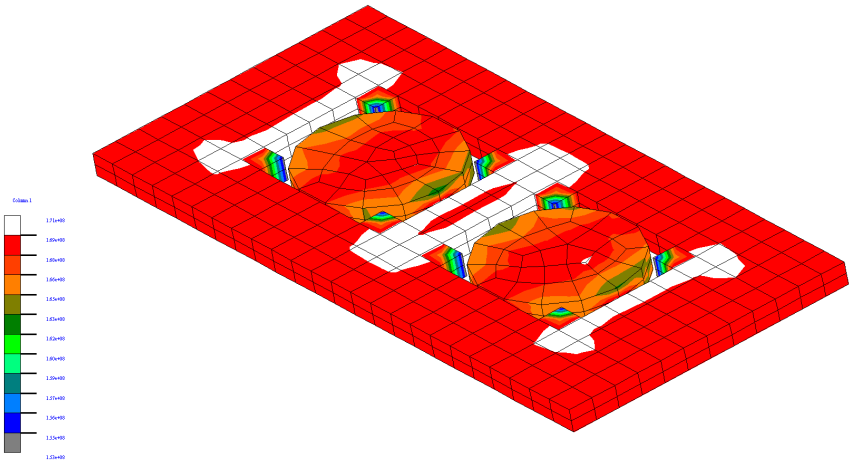

(a) σ_{11} using suggested penalty parameter

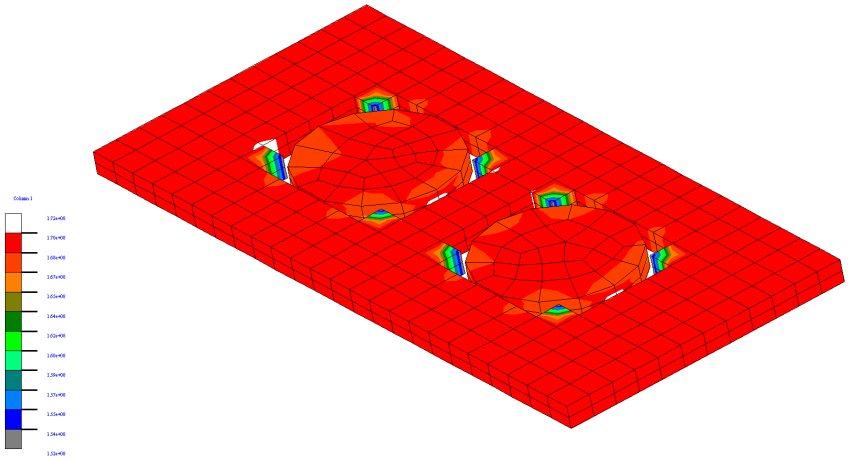

(b) σ_{11} using converged penalty parameter

Figure 5.33: Contour plots of σ_{11} for single property IMM two-inclusion models

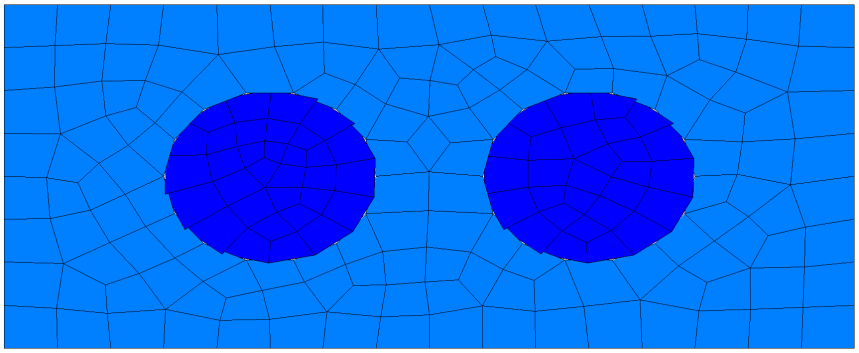

Figure 5.34: IMM rotated two-inclusion mesh

meshed surfaces without the use of the X3D8 elements.

5.2.4.1 Mesh

The modified two-inclusion mesh was made from the coarse conventional mesh by slightly rotating the inclusions about the out of plane axis. Since the mesh was initially compatible, this causes the surface meshes to become incompatible. In addition since the inclusions are circular, the finite element mesh is a linear approximation of the circle leading to a faceted perimeter of the inclusion mesh. This is also true for the cutout in the matrix. Therefore, rotating this faceted surface causes equal amounts of interpenetration and gaps between the two mesh entities. So, in addition to rotating the inclusions, their in-plane coordinates were also scaled by a small factor (in an axisymmetric fashion), to get rid of all of the gaps and increase the size of the interpenetrations. The resulting modified mesh with the rotated inclusions is shown in Figure 5.34.

5.2.4.2 Convergence

A convergence study of the predicted effective modulus with respect to penalty parameter was conducted to evaluate the converged penalty value. The results are presented in Table 5.7, and the convergence of the predicted modulus is plotted

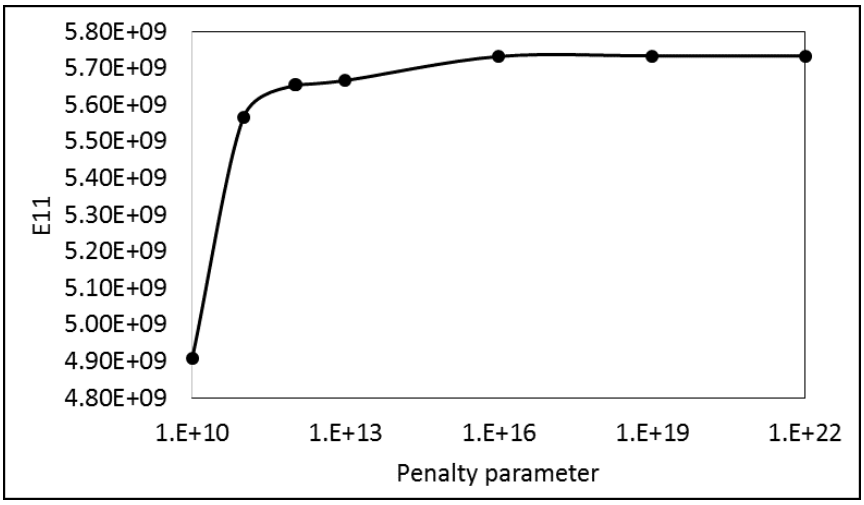

Figure 5.35: Convergence of predicted modulus with respect to penalty parameter for IMM rotated two-inclusion model

Table 5.7: Key metrics from IMM Rotated model

PP	Modulus (GPa)	Error	Peak σ_{11} (Pa)	Error	v_{10}^{Max} σ_{11}	Error
1.052E12	5.6544	0.18	1.4015E8	0.71	12.34	168.26
1E16	5.7323	1.56	1.4527E8	2.81	19.62	326.52

in Figure 5.35. The curve of the effective modulus convergence exhibits the same behavior as in the regular IMM two-inclusion analysis for the coarse mesh.

5.2.4.3 Locations of stress concentrations

The locations of the stress concentrations for the IMM rotated two-inclusion analysis are shown through the contour plots in Figure 5.36, for the suggested penalty value, and Figure 5.37, for the converged. In Figure 5.37b and Figure 5.37d it can be seen that the IMM results match the conventional results extremely well for the suggested penalty parameter. The peak tensile stress concentration on the inclusion, labeled A in Figure 5.37d, is slightly larger than in the conventional plot. This is attributable to the rotation of the inclusion such that there is no longer a node

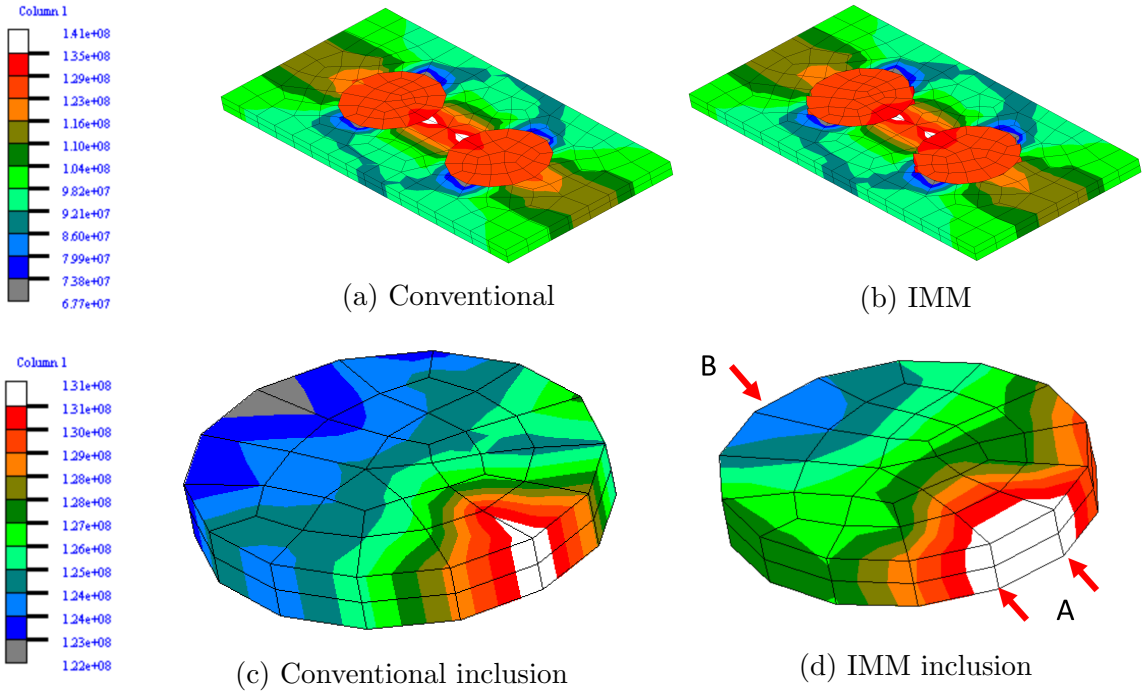

Figure 5.36: Contour plots of σ_{11} for IMM rotated two-inclusion model using suggested penalty

at the point closest to the adjacent inclusion. Rather, there are two nodes spread equidistantly from this location, causing the peak stress value to be interpolated to each. This slightly larger concentration is apparent in the higher v_{10}^{Max} value for the IMM results, as well as the stress volume distribution curve. The contour plots for the converged penalty value show that the penalty connection is likely too stiff, given that there are small interpenetrations in the mesh.

5.2.4.4 Stress volume distributions

The stress volume distributions of σ_{11} within the matrix and inclusions are plotted for the conventional and IMM rotated two-inclusion models in Figure 5.38 and Figure 5.39. Like before when the IMM code was updated and the errors were fixed, the curves in these plots are nearly identical, so they are supplemented with reduced

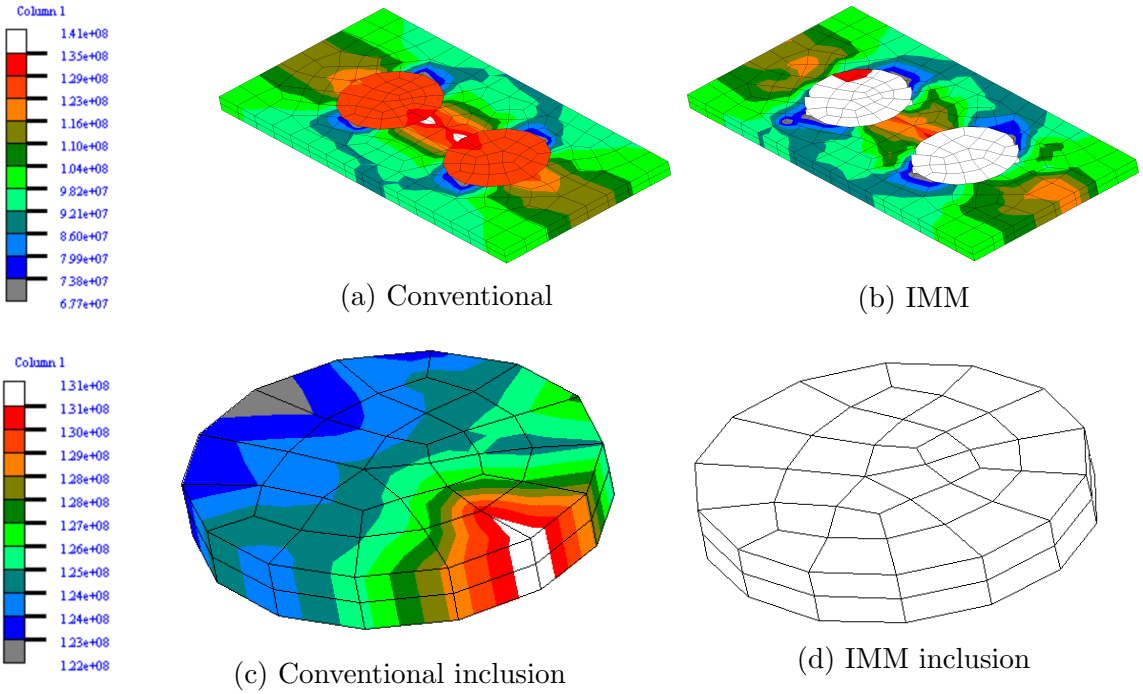

(a) Conventional

(b) IMM

(c) Conventional inclusion

(d) IMM inclusion

Figure 5.37: Contour plots of σ_{11} for IMM rotated two-inclusion model using converged penalty

range figures. These zoomed in figures are magnified on the top 20% stress values. The plot for the matrix, Figure 5.38b, show almost identical distributions. The plot for the inclusion, Figure 5.39b, echoes the contour plot in that a higher amount of the material gets close to the peak stress.

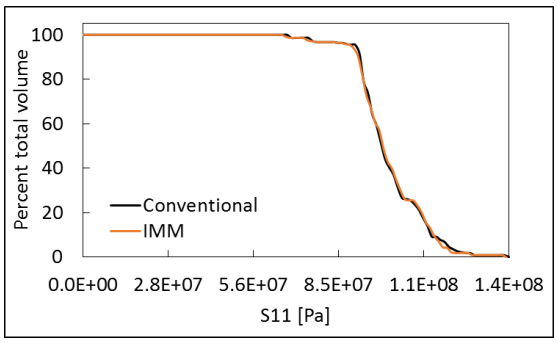

(a) Full range

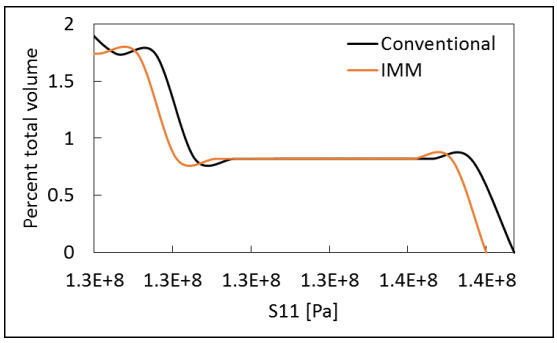

(b) Zoomed in view

Figure 5.38: Volume distributions of σ_{11} within matrix

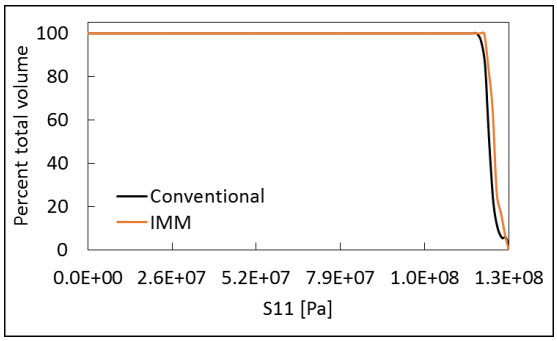

(a) Full range

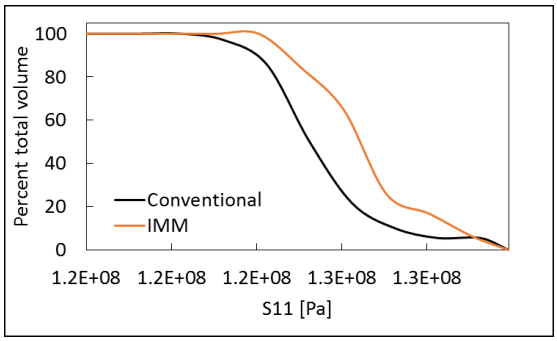

(b) Zoomed in view

Figure 5.39: Volume distributions of σ_{11} within inclusion

6. CONCLUSIONS

The objective of this research was to evaluate the performance of the Independent Mesh Method. This required a suitable strategy for drawing a comparison, which was addressed by the careful selection and construction of analysis configurations that required no unnecessary logistical differences between their use in a conventional analysis and their use in the IMM analysis. Both of the configurations chosen satisfy this requirement and were proven to produce identical results when the characteristics of the IMM were not used. In addition, a sufficient set of metrics was required to evaluate the comparison. The metrics used herein ranged from results such as the predicted effective elastic modulus, to key stress values such as the peak stresses and their locations, to very detailed analyses of the distribution of stresses throughout the material volumes.

It was shown that the initial version of the IMM contained significant coding issues. These issues were corrected, and the results from the final version of the IMM code were presented. For the plain weave analysis, the results from the IMM compared quite well to the conventional benchmark, although there were lingering differences that were further investigated using the simplified two-inclusion configuration. A significant drawback of the IMM is the absence of stress information in the X3D8 elements, namely the regions of the matrix which interface with the tows. In textile composites, it is commonly known that when normalized by strength, the matrix sees the highest normalized stresses. This occurs, of course, at its interfaces with the volumes occupied by the tows. In its current state, the only accessibility to this information in an IMM analysis is through interpolation of surrounding results to points near the matrix-tow interface. The coordinates of these points are not

provided, nor are the stresses at the integration points within the X3D8 elements, so it is impossible to reproduce this information, or use it in post processing.

With the use of the two-inclusion model it was shown that the penalty parameter has an extreme effect on the results. In addition, the suggested penalty parameter is not always within the range of converged penalty parameters. Using either the suggested or the minimum converged penalty value is shown to produce results with significant distortions in the stress distributions near the material interfaces. The simplified model using a single material property shows exactly where the locations that cause these distortions are, although it is difficult to characterize the properties of the mesh that make these locations different from the others. To this end, the simplified model using rotated inclusions, without the use of X3D8 elements, provides insight into what factors are causing the penalty connection to disrupt the stress fields in the other models. Since the IMM rotated two-inclusion model compares much better with the conventional than the regular or single property models, it can be determined that either penalty connections involving X3D8 elements, or penalty connections involving significantly overlapping elements are the source of the error.

This research has helped to improve the IMM , as well as gain insight into its weaknesses, and possible issues. Future work on this subject should involve modification of the penalty scheme, or perhaps an alternative method for imposing displacement continuity between the meshes, to remove the errors it is currently causing.

REFERENCES

[1] E.G. Zhou, D.H. Mollenhauer, and E.V. Iarve. A realistic 3d textile geometric model. In *Proceedings of 17th International Committee on Composite Materials*, July 2009.

[2] J.D. Whitcomb. Three-dimensional stress analysis of plain weave composites. *Composite Materials Fatigue and Fracture*, 3:417–438, 1991.

[3] C.D. Chapman and J.D. Whitcomb. Effect of assumed tow architecture on predicted moduli and stresses in plain weave composites. *Journal of Composite Materials*, 29(16):2134–2159, 1995.

[4] M.K. Ballard, W.R. McLendon, and J.D. Whitcomb. The influence of microstructure randomness on prediction of fiber properties in composites. *Journal of Composite Materials*, 48(29):3605–3620, 2014.

[5] E.G. Zhou, X. Sun, and Y. Wang. Multi-chain digital element analysis in textile mechanics. *Composites Science and Technology*, 64:239–244, 2004.

[6] Y. Wang and X. Sun. Digital-element simulation of textile processes. *Composites Science and Technology*, 61:311–319, 2001.

[7] E.V. Iarve, D.H. Mollenhauer, E.G. Zhou, T. Breitzman, and T.J. Whitney. Independent mesh method-based prediction of local and volume average fields in textile composites. *Composites: Part A*, 40:1880–1890, 2009.

[8] J.D. Whitcomb, C.D. Chapman, and X. Tang. Derivation of boundary conditions for micromechanics analyses of plain and satin weave composites. *Journal of Composite Materials*, 34(9):724–747, 2000.

[9] D.M. Blackketter, D.E. Walrath, and A.C. Hansen. Modeling damage in a plain weave fabric-reinforced composite material. *Journal of Composites Technology & Research*, 15(2):136–142, 1993.

[10] J.D. Whitcomb and K. Srirengan. Effect of various approximations on predicted progressive failure in plain weave composites. *Composite Structures*, 34:13–20, 1996.

[11] H. Thom. Finite element modeling of plain weave composites. *Journal of Composite Materials*, 33(16):1491–1510, 1999.

[12] A. Dasgupta, R.K. Agarwal, and S.M. Bhandarkar. Three-dimensional modeling of woven-fabric composites for effective thermo-mmechanical and thermal properties. *Composites Science and Technology*, 56:209–223, 1996.

[13] V. Carvelli and C. Poggi. A homogenization procedure for the numerical analysis of woven fabric composites. *Composites: Part A*, 32:1425–1432, 2001.

[14] X. Tang and J.D. Whitcomb. General techniques for exploiting periodicity and symmetries in micromechanics analysis of textile composites. *Journal of Composite Materials*, 37(13):1167–1189, 2003.

[15] D. Goyal, X. Tang, J.D. Whitcomb, and A.D. Kelkar. Effect of various parameters on effective engineering properties of 2 x 2 braided composites. *Mechanics of Advanced Materials and Structures*, 12:113–118, 2005.

[16] D. Goyal and J.D. Whitcomb. Analysis of stress concentrations in 2 x 2 braided composites. *Journal of Composite Materials*, 40(6):533–546, 2006.

[17] K. Woo and J.D. Whitcomb. Three-dimensional failure analysis of plain weave textile composites using a global/local finite element method. *Journal of Composite Materials*, 30(9):984–1003, 1996.

[18] K. Woo and J. D. Whitcomb. Macro finite element using subdomain integration. *Communications in Numerical Methods in Engineering*, 9:937–949, 1993.

[19] B.N. Cox, W.C. Carter, and N.A. Fleck. A binary model of textile composites-I. Formulation. *Acta Metallurgica et Materialia*, 42(10):3463–3479, 1994.

[20] J. Xu, B.N. Cox, M.A. McGlockton, and W.C. Carter. A binary model of textile composites-II. The elastic regime. *Acta Metallurgica et Materialia*, 43(9):3511–3524, 1995.

[21] Q. Yang and B.N. Cox. Spatially averaged local strains in textile composites via the binary model formulation. *Journal of Engineering Materials and Technology*, 125:418–425, 2003.

[22] Q.D. Yang and B.N. Cox. Predicting failure in textile composites using the binary model with gauge-averaging. *Engineering Fracture Mechanics*, 77:3174–3189, 2010.

[23] W.G. Jiang, S.R. Hallett, and M.R. Wisnom. Development of domain superposition technique for the modelling of woven fabric composites. In P.P. Camanho, C.G. Dávila, S.T. Pinho, and J.J.C. Remmers, editors, *Mechanical Response of Composites*, chapter 14, pages 281–291. Springer Netherlands, Dordrecht, 2008.

[24] J. Fish, S. Markolefas, R. Guttal, and P. Nayak. On adaptive multilevel superposition of finite element meshes for linear elastostatics. *Applied Numerical Mathematics*, 14:135–164, 1994.

[25] A.V. Kumar, R. Buria, S. Padmanabhan, and L. Gu. Finite element analysis using nonconforming mesh. *Journal of Computing and Information Science in Engineering*, 8:031005–1–11, 2008.

[26] A.V. Kumar, S. Padmanabhan, and R. Burla. Implicit boundary method for finite element analysis using non-conforming mesh or grid. *International Journal for Numerical Methods in Engineering*, 74:1421–1447, 2008.

[27] S.A. Tabatabaei, S.V. Lomov, and I. Verpoest. Assessment of embedded element technique in meso-FE modelling of fibre reinforced composites. *Composite Structures*, 107:436–446, 2014.

[28] S.A. Tabatabaei and S.V. Lomov. Eliminating the volume redundancy of embedded elements and yarn interpenetrations in meso-finite element modelling of textile composites. *Computers & Structures*, 152:142–154, 2015.

[29] F.T. Peirce. The geometry of cloth structure. *Journal of the Textile Institute*, 28(3):45–97, 1937.

[30] A. Kemp. An extension of peirce's cloth geometry to the treatment of non-circular threads. *Journal of the Textile Institute*, 49:T44–T48, 1958.

[31] J.W.S. Hearle and W.J. Shanahan. An energy method for calculations in fabric mechanics part I: Principles of the method. *Journal of the Textile Institute*, 69(4):81–91, 1978.

[32] J.W.S. Hearle and W.J. Shanahan. An energy method for calculations in fabric mechanics part II: Exampls of application of the method to woven fabrics. *Journal of the Textile Institute*, 69(4):92–100, 1978.

[33] G. Hivet and P. Boisse. Consistent 3d geometric model of fabric elementary cell. Application to a meshing preprocessor for 3d finite element analysis. *Finite Element Analysis and Design*, 42:25–49, 2005.

[34] F. Robitaille, B.R. Clayton, A.C. Long, B.J. Souter, and C.D. Rudd. Geometric modelling of industrial preforms: woven and braided textiles. *Proceedings of the Institution of Mechanical Engineers, Part L*, 213:69–83, 1999.

[35] F. Robitaille, B.R. Clayton, A.C. Long, B.J. Souter, and C.D. Rudd. Geometric modelling of industrial preforms: warp-knitted textiles. *Proceedings of the Institution of Mechanical Engineers, Part L*, 214:71–90, 2000.

[36] F. Robitaille, A.C. Long, and C.D. Rudd. Geometric modelling of textiles for prediction of composite processing and performance characteristics. *Plastics, Rubber and Composites*, 31(2):66–75, 2002.

[37] F. Robitaille, A.C. Long, I.A. Jones, and C.D. Rudd. Automatically generated geometric descriptions of textile and composite unit cells. *Composites: Part A*, 34:303–312, 2003.

[38] H.J. Kim and C.C. Swan. Voxel-based meshing and unit-cell analysis of textile composites. *International Journal for Numerical Methods in Engineering*, 56:977–1006, 2003.

[39] H.J. Kim and C.C. Swan. Algorithms for automated meshing and unit cell analysis of periodic composites with hierarchical tri-quadratic tetrahedral elements. *International Journal for Numerical Methods in Engineering*, 58:1683–1711, 2003.

[40] E. Potter, S.T. Pinho, P. Robinson, L. Iannucci, and A.J. McMillan. Mesh generation and geometrical modelling of 3d woven composites with variable tow cross-sections. *Computational Materials Science*, 51:103–111, 2012.

[41] S.K. Boyd and R. Muller. Smooth surface meshing for automated finite element model generation from 3d image data. *Journal of Biomechanics*, 39:1287–1295, 2006.

[42] M. Sherburn, A. Long, A. Jones, J. Crookston, and L. Brown. Prediction of textile geometry using an energy minimization approach. *Journal of Industrial Textiles*, 41(4):345–369, 2011.

[43] S.V. Lomov, A.V. Gusakov, G. Huysmans, A. Prodromou, and I. Verpoest. Textile geometry preprocessor for meso-miechanical models of woven composites. *Composites Science and Technology*, 60:2083–2095, 2000.

[44] S.V. Lomov, G. Huysmans, and I. Verpoest. Hierarchy of textile structures and architecture of fabric geometric models. *Textile Research Journal*, 71(6):534–543, 2001.

[45] I. Verpoest and S.V. Lomov. Virtual textile composites software wisetex: Integration with micro-mechanical, permeability and structural analysis. *Composites Science and Technology*, 65:2563–2574, 2005.

[46] S.V. Lomov, D.S. Ivanov, I. Verpoest, M. Zako, T. Kurashiki, H. Nakai, and S. Hirosawa. Meso-FE modelling of textile composites: Road map, data flow and algorithms. *Composites Science and Technology*, 67:1870–1891, 2007.

[47] S.V. Lomov, G. Perie, D.S. Ivanov, I. Verpoest, and D. Marsal. Modeling three-dimensional fabrics and three-dimensional reinforced composites: challenges and solutions. *Textile Research Journal*, 81(1):28–41, 2011.

[48] S.V. Lomov, I. Verpoest, J. Cichosz, C. Hahn, D.S. Ivanov, and B. Verleye. Meso-level textile composites simulations: open data exchange and scripting. *Journal of Composite Materials*, 48(5):621–637, 2014.

[49] F. Desplentere, S.V. Lomov, D.L. Woerdeman, I. Verpoest, M. Wevers, and A. Bogdanovich. Micro-CT characterization of variability in 3d textile architecture. *Composites Science and Technology*, 65:1920–1930, 2005.

[50] A. Drach, B. Drach, and I. Tsukrov. Processing of fiber architecture data for finite element modeling of 3d woven composites. *Advances in Engineering Software*, 72:18–27, 2014.

[51] G. Grail, M. Hirsekorn, A. Wendling, G. Hivet, and R. Hanbli. Consistent finite element mesh generation for meso-scale modeling of textile composites with preformed and compacted reinforcements. *Composites: Part A*, 55:143–151, 2013.